

Unsteady motions in the turbulent separation bubble of a two-dimensional wing

Sen Wang¹ and Sina Ghaemi^{1,†}

¹Department of Mechanical Engineering, University of Alberta, Edmonton, Alberta T6G 2R3, Canada

(Received 6 February 2022; revised 1 July 2022; accepted 5 July 2022)

The unsteadiness of a turbulent separation bubble (TSB) formed close to the trailing edge of a two-dimensional wing was investigated using time-resolved particle image velocimetry. The angle of attack was set to 9.7° and the chord-based Reynolds number was 720 000. The TSB consisted of two shear layers and formed a triangular shape in the streamwise–wall-normal plane. The vertices of this triangle consisted of an intermittent detachment point, a fixed corner close to the airfoil trailing edge and an intermittent endpoint in the wake region. The velocity field had three energetic regions each with different Strouhal numbers (St_l): (a) an upstream turbulent boundary layer (TBL) with $St_l = 0.1$ to 4, (b) a TSB with $St_l = 0.03$ to 0.08 and (c) two shear layers with $St_l = 0.4$ to 0.8. The low-frequency motions in the TSB consisted of large zones of positive and negative streamwise velocity fluctuation that were several times wider than the large-scale structures of the upstream TBL. These zones forced an undulation of the separation line and were attributed to Görtler structures. They were also correlated with the velocity fluctuations between the two shear layers. The breathing motion of the TSB occurred at $St_l = 0.05$. This breathing correlated with the location of the TSB endpoint and the flapping of the upper shear layer. The detachment point of the TSB featured broad fluctuations and did not demonstrate a strong correlation with the breathing motion.

Key words: boundary layer separation, turbulent boundary layers, separated flows

1. Introduction

Trailing-edge (TE) separation refers to the detachment of a turbulent boundary layer (TBL) from the aft section of an airfoil. The detachment occurs due to an adverse pressure gradient (APG) and typically on thick airfoils operating at high angles of attack, α . The separated flow features an intermittent separation front and a turbulent separation bubble (TSB) that extends up to the airfoil TE (Ma, Gibeau & Ghaemi 2020). Although this type

† Email address for correspondence: ghaemi@ualberta.ca

of TSB only covers the aft portion of the airfoil, the generated lift fluctuations are as strong as those generated by leading-edge separation (Broeren & Bragg 1998). In one of the early investigations of TE separation, Zaman, McKinzie & Rumsey (1989) noted that a significant part of the energy of the fluctuations is at frequencies that are an order of magnitude smaller than the vortex shedding frequency. Characterizing and understanding the source of this low-frequency fluctuation for TE separation is the focus of the current investigation.

A broader look at the investigations of TSBs shows that the low-frequency fluctuations are not limited to pressure-induced separation over airfoils. Earlier observations of this phenomenon considered TSBs generated by geometric singularities – a flow category known as geometry-induced TSBs. For example, low-frequency oscillations were reported in TSBs formed by flat plates mounted perpendicular to the free stream (Castro & Haque 1987), two- and three-dimensional surface-mounted blocks (Castro 1981), backward- and forward-facing steps (Eaton & Johnston 1982; Pearson, Goulart, & Ganapathisubramani 2013) and the leading edge of blunt plates (Kiya & Sasaki 1983; Cherry, Hiller & Latour 1984). In these investigations, the Strouhal number, St , of the low-frequency motions was found to range from 0.08 to 0.2, while the vortex shedding process was at higher frequencies of $St = 0.5$ to 1.0. Here, St is defined as fL/U_∞ , where f is frequency, U_∞ is free-stream velocity and L is a relevant length scale such as the step height or plate thickness.

In geometry-induced TSBs, the low-frequency oscillations are attributed to the wall-normal motions of the detached shear layers and are therefore referred to as ‘flapping’ motions (Eaton 1980). For the TSB of a backward-facing step, Eaton & Johnston (1982) hypothesized that the flapping motion is generated due to an instantaneous imbalance between fluid entrainment into the shear layer and its reinjection into the recirculating region. The imbalance occurs at a frequency lower than the vortex shedding frequency and has been associated with several mechanisms such as the modulation, pairing, or interruption of the vortex shedding process (Cherry *et al.* 1984; Kiya & Sasaki 1985; Driver, Seegmiller & Marvin 1987). In contrast, Pearson *et al.* (2013) considered the TSB of a forward-facing step and attributed the flapping motion to the perturbations induced by the upstream TBL. These perturbations originate from the streamwise-elongated low- and high-velocity motions of TBLs (Adrian, Meinhart & Tomkins 2000; Hutchins & Marusic 2007). Pearson *et al.* (2013) observed that the TSB expanded or contracted simultaneously in both the streamwise and wall-normal directions. Therefore, the flapping motion led to an overall expansion/contraction of the TSB cross-section, which is known as the ‘breathing’ motion. The apparent discrepancy between the two mechanisms proposed by Eaton & Johnston (1982) and Pearson *et al.* (2013) can be due to the different flow configurations used in their experiments. The TSB of Pearson *et al.* (2013) was located upstream of the forward-facing step and had an intermittent separation point while the TSB of Eaton & Johnston (1982) was downstream of the backward-facing step and had an intermittent reattachment. These observations suggest that the mechanism responsible for the breathing motion in TSBs is configuration dependent.

Low-frequency breathing motions are also present in TSBs induced by shock waves. For shock-induced TSBs, the St of the low-frequency motions varies from 0.02 to 0.05 (Dussauge, Dupont, Debiève 2006). Here, the length scale used for calculating the St is defined based on the interaction length between the shock wave and the boundary layer. However, despite using a different length scale, the St of the breathing motions is at least an order of magnitude smaller than the characteristic St of the flow based on the free-stream velocity U_∞ and boundary layer thickness δ , i.e. $f\delta/U_\infty$

(Dolling 2001). According to a review by Clemens & Narayanaswamy (2014), the low-frequency unsteadiness in shock-induced TSBs can originate from either upstream or downstream of the TSB. When the interaction between the shock wave and TBL is weak and the TSB is small, the breathing motion has been attributed to a combination of local and global velocity fluctuations within the incoming TBL (Ganapathisubramani, Clemens & Dolling 2009, Humble, Scarano & Van Oudheusden 2009). In contrast, for the stronger shock wave–TBL interactions of larger TSBs, the consensus is that a downstream mechanism, due to the imbalance of entrainment and recharge rates of the shear layer, generates the breathing motion (Wu & Martin 2008; Piponniau *et al.* 2009). Although there are fundamental differences between supersonic and subsonic flows, Weiss, Mohammed-Taifour & Schwaab (2015) and Mohammed-Taifour & Weiss (2021) noted that their breathing motion may share a similar mechanism.

In pressure-induced TSBs, several experimental and numerical investigations observed low-frequency unsteadiness that was not associated with the vortex shedding process. An early investigation by Patrick (1987) generated a TSB on a flat plate using a converging–diverging wall. This induced an APG followed by a favourable pressure gradient (FPG) on the opposing flat wall. They reported non-periodic flow unsteadiness at frequencies ranging from 5 to 50 Hz, which is equivalent to $St_l = 0.2$ to 2. Here, St_l is defined based on the mean length of the separation bubble, l . The TSB of Dianat & Castro (1991) demonstrated non-periodic low-frequency oscillations centred at $St_l = 0.5$. Dianat & Castro (1991) generated the TSB by applying suction above a flat plate, which resulted in an upstream FPG followed by a downstream APG. For the TSB of an airfoil at the onset of stall, Zaman *et al.* (1989) observed oscillations at a small St of approximately 0.02. They defined St based on the frontal projection of the chord length, c . Na & Moin (1998) carried out direct numerical simulation (DNS) of a TSB induced on a flat plate using an APG followed by a downstream FPG. Visual inspection of instantaneous pressure fields showed low-frequency structures at $St = 0.003$ to 0.01, where St was defined based on the displacement thickness of the upstream TBL. However, the objective of these investigations was not to characterize the low-frequency motions, and some observations might be inaccurate due to the limitations of experimental and numerical techniques.

In a detailed experimental investigation, Weiss *et al.* (2015) characterized the unsteady motions of a TSB induced on a flat plate using an opposing converging–diverging wall. They observed low-frequency fluctuations at $St_l = 0.01$ due to the breathing motion, while the vortex shedding was at a higher frequency of $St_l = 0.35$. In contrast, a recent DNS by Wu, Meneveau & Mittal (2020) showed that a TSB induced only by an APG on a flat plate exhibits low-frequency motions at $St_l = 0.45$, which was 2–3 times smaller than the St of the vortex shedding process. In this numerical investigation, when the TSB was induced using an APG followed by FPG, the low-frequency fluctuations disappeared. Wu *et al.* (2020) attributed this behaviour to the forced attachment of the shear layer by the imposed FPG. They also commented that the TSB induced solely by an APG is a better representative of TSBs on airfoils since the shear-layer attachment occurs gradually due to the turbulent diffusion of momentum. However, this flow configuration is still not a true representation of TE separation. As it is shown in the current investigation, TE separation forms a triangular-shaped TSB that is different from the dome-shaped TSBs that form on flat plates. The first vertex of the triangular-shaped TSB is the intermittent separation point, the second vertex is pinned at the trailing edge and the third vertex extends into the wake region downstream of the TE. The TE separation also has an additional shear layer that forms by the separation of the pressure-side boundary layer at the airfoil TE. This

shear layer plays an important role in fluid entrainment and wake dynamics (Cicatelli & Sieverding 1997; Ozkan 2021).

There are several differences between the observations of Wu *et al.* (2020) using DNS and the experiments of Weiss *et al.* (2015). First, the low-frequency oscillations in Wu *et al.* (2020) were at $St_l = 0.45$, while Weiss *et al.* (2015) observed the low-frequency motions at $St_l = 0.01$. Second, Wu *et al.* (2020) observed the low-frequency oscillations close to the reattachment location, whereas Weiss *et al.* (2015) detected them near the separation location. Third, Wu *et al.* (2020) did not observe any low-frequency motion when a suction–blowing boundary condition was used for generating the TSB, which is similar to the APG followed by FPG boundary condition applied by Weiss *et al.* (2015). These apparent contradictions can be explained by noting the differences in the flow conditions between studies. The DNS of Wu *et al.* (2020) was carried out using a TBL at a momentum thickness Reynolds number of $Re_\theta = 490$, which is quite different from the $Re_\theta = 5000$ TBLs studied by Weiss *et al.* (2015). At such high Re_θ , the TBL contains large-scale motions that populate the logarithmic and lower wake regions of high-Reynolds-number TBLs (Guala, Hommema & Adrian 2006; Hutchins & Marusic 2007). Another striking difference is the longer extent of the reattachment region featured by the TSB of Wu *et al.* (2020). More specifically, the region between forward-flow fractions of $\gamma = 0.2$ and 0.8 extended over a length equal to l in Wu *et al.* (2020), while this zone was approximately equal to $0.2l$ in the studies of in Weiss *et al.* (2015). The longer reattachment length in Wu *et al.* (2020) was due to the lack of a FPG boundary condition, thus allowing the separated shear layer to gradually attach. Finally, computational limitations may also contribute to the discrepancies. The smallest St_l resolved in Wu *et al.* (2020) was 0.2 , which does not allow inspection of lower frequencies.

The mechanisms that are proposed for the low-frequency fluctuations in pressure-induced TSBs are similar to those suggested for geometry- and shock-induced TSBs. Na & Moin (1998) associated the low-frequency fluctuations with the intermittency of the reattachment point due to large arch-type vortical structures. The latter structures potentially formed from the agglomeration of smaller Kelvin–Helmholtz vortices. Since the arch-type vortices transport fluid in the wall-normal direction, this observation is consistent with the proposed mechanism based on the imbalance between fluid entrainment and reinjection in geometry-induced TSBs. The recent DNS of Wu *et al.* (2020) also demonstrated large-scale vorticity packets that resulted in intermittent displacements of the reattachment location and flow fluctuations at $St_l = 0.45$. Using dynamic mode decomposition (DMD), Wu *et al.* (2020) observed streamwise-elongated structures that cover the full length of the TSB and break down into large-scale vorticity packets. They suggested that Görtler-type instabilities amplify the perturbations of the incoming TBL and generate the streamwise-elongated structures. The latter hypothesis also points to the incoming TBL as a source for the low-frequency fluctuations.

In a recent experimental investigation, Mohammed-Taifour & Weiss (2021) showed that transient forcing of the incoming TBL using pulsed-jet actuators first influences the separation point and then the reattachment location. They also observed that the time required for the flow to recover from the controlled state was of the same order of magnitude as the time scale of the low-frequency breathing motions. Therefore, Mohammed-Taifour & Weiss (2021) suggested that the perturbations of the upstream TBL generate the breathing motion by first affecting the separation point and then indirectly affecting the reattachment point through large-scale pressure fluctuations. The effect of TBL structures on the separation front has been demonstrated by two recent investigations. Eich & Kähler (2020) demonstrated that large-scale motions of the incoming TBL modulate the separation line. By investigating the TSB of a flat plate, they showed that

large high-speed motions within the incoming TBL push the separation location in the downstream direction while large low-speed motions result in an upstream displacement of the separation location. Ma *et al.* (2020) characterized the topology of these interactions in TE separation and observed that the instantaneous separation front comprises small-scale structures that resembled the ‘stall cells’.

The current investigation characterizes flow unsteadiness of the TE separation formed on a NACA 4418 airfoil at a pre-stall angle of attack. The main objective is to characterize the low-frequency motions and investigate their formation mechanism. In particular, we probe the relationship between the low-frequency flow motions with the incoming TBL and the downstream vortex shedding. Time-resolved planar particle image velocimetry (PIV) measurements were carried out in a streamwise–wall-normal plane at the midspan of the wing and a wall-parallel streamwise–spanwise plane close to the wing surface.

The manuscript first characterizes the TSB using first- and second-order turbulence statistics. Spectral analysis is then performed to characterize the unsteadiness of the flow motions. This is followed by identifying the spatial and temporal scales of the motions using two-point correlations, and the energetic motions using spectral proper orthogonal decomposition (SPOD). Finally, the mechanism of the breathing motion is scrutinized by correlating the cross-sectional area of the TSB with the displacements of the detachment and endpoint of the TSB.

2. Experimental methodology

2.1. Wind tunnel and airfoil

The experiments were carried out in a large two-story, closed-loop wind tunnel at the University of Alberta that is shown schematically in [figure 1\(a\)](#). The nozzle had a contraction ratio of 6.3 : 1 which led to a test section with a cross-section of $1.2 \times 2.4 \text{ m}^2$. The experiments were conducted at a free-stream velocity of $U_\infty = 11.2 \text{ m s}^{-1}$, resulting in a turbulence intensity of 0.34 % and a maximum non-uniformity of 0.5 % across the test section, as demonstrated by previous measurements in the facility (Gibeau, Gingras, & Ghaemi 2020). Spectral analysis of the free-stream flow shows an energetic peak at approximately 20 Hz (details are available in the [Appendix](#)). A two-dimensional wing with an aspect ratio of 1.2 was mounted vertically within the test section with its spanwise ends mounted flush to the ceiling and floor. The wing featured a NACA 4418 airfoil cross-section and a chord length of $c = 975 \text{ mm}$. The Reynolds number based on the free-stream velocity and the chord of the wing was 720 000. A full-span trip wire with a 1 mm diameter was installed at $0.2c$ downstream of the leading edge to ensure a uniform laminar-to-turbulent transition across the wingspan. The small curvature of the airfoil profile from $0.67c$ to the TE of the suction side was replaced with a straight line. This small modification resulted in a flat TE section, which is suitable for wall-parallel PIV measurements (Wang & Ghaemi 2021). The angle of attack, α , of the wing was set to 9.7° resulting in the mean separation point being located 130 mm ($0.13c$) upstream of the TE. The origin of the coordinate system, which is shown using point O in [figure 1\(b\)](#), was placed at the TE. The streamwise, wall-normal and spanwise directions are represented by x , y and z , and the corresponding instantaneous velocity components using U , V and W , respectively. The fluctuating components are indicated by u , v and w .

Differential pressure transducers were used for measuring the pressure distribution close to the TE of the wing. Twelve pinholes with diameters of 0.5 mm were evenly distributed between $x/c = -0.31$ and -0.08 along the midspan of the wing. Flexible tubes of 2.5 m

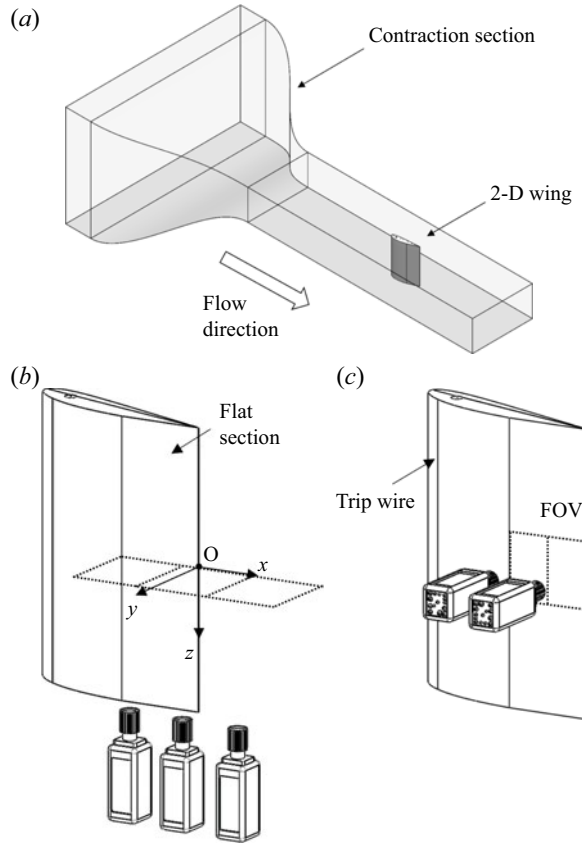


Figure 1. (a) The two-dimensional wing is vertically installed in the wind tunnel with its spanwise ends flush to the wind tunnel walls. (b) Time-resolved planar PIV in a streamwise–wall-normal plane at the midspan of the wing using three high-speed cameras. The origin of the measurement system (point O) is at the TE of the midspan plane. (c) Time-resolved planar PIV in a wall-parallel plane using two high-speed cameras.

length were used to connect the pinholes to the transducers (Ashcroft IXLdp), which could measure a maximum differential pressure of 62 Pa and featured $\pm 0.25\%$ accuracy. The output voltage was recorded at 100 Hz using a 16-bit National Instrument data acquisition device (USB-6218) over a duration of 120 s. The differential pressure of the pinholes, Δp , was measured with respect to the static pressure at the most upstream pinhole located at $x/c = -0.31$. These pressure differences were normalized as $2(\Delta p)/\rho U_\infty^2$ where ρ is air density at 23 °C.

2.2. Time-resolved planar PIV

For time-resolved planar PIV in the x – y plane of the midspan, three high-speed cameras (v611 Phantom) were employed to simultaneously capture a large field of view (FOV) that covered the entire flat section of the airfoil and the wake region. The FOV is shown with dashed lines in figure 1(b). The camera sensor featured 1280×800 pixels with a pixel size of $20 \times 20 \mu\text{m}^2$. The frame rate was set to 4.5 kHz to obtain time-resolved PIV images in single-frame mode. The cameras were equipped with macro lenses (Sigma) each with a focal length of $f = 105$ mm. The aperture size was maximized to a setting of $f/2.8$ to increase the light intensity within the images. Each camera imaged at a digital

resolution of approximately 0.19 mm pix^{-1} , resulting in a FOV of $243 \times 152 \text{ mm}^2$ in the x and y directions, respectively. The combined FOV had dimensions of $660 \times 145 \text{ mm}^2$ in the x and y directions and was obtained using vector stitching. The illumination was provided by a dual-cavity high-speed Nd:YLF laser (Photonics Industries, DM20-527DH) capable of 20 mJ per pulse at 1 kHz. A combination of spherical and cylindrical lenses was used to produce a streamwise–wall-normal laser sheet with an average thickness of 1.5 mm across the entire FOV. To reduce the glaring line due to the reflection of the laser from the wing surface, the laser light was directed from the upstream side of the wing and the edge of the laser sheet was approximately parallel to the flat section. The air flow was seeded using $1 \text{ }\mu\text{m}$ droplets generated by a fog generator. In total, 15 sets of time-resolved data, each consisting of 5464 single-frame images, were collected at 4.5 kHz. To improve the signal-to-noise ratio (SNR), the minimum intensity of the ensemble was subtracted from each image, which was then normalized with the average intensity. The vector fields were obtained using a sliding-sum-of-correlation method which averaged the correlations from three successive image pairs (Ghaemi, Ragni & Scarano 2012). The final interrogation window was 32×32 pixels ($6 \times 6 \text{ mm}^2$) with 75 % overlap. The vector fields contained approximately 2 %–3 % spurious vectors due to the strong three-dimensionality of the separated flow, mostly observed downstream of the TE. Universal outlier detection (Westerweel & Scarano 2005) and bilinear interpolation were applied to remove and replace these spurious vectors. All image processing was carried out using DaVis 8.4 (LaVision GmbH).

The spanwise dynamics of the TSB was investigated using time-resolved planar PIV in a wall-parallel streamwise–spanwise plane. This plane was located 4 mm away from the wing surface and was imaged using two cameras, as shown in the schematic of figure 1(c). The wall-normal distance was needed to reduce the scattered light from the surface in the PIV images and obtain a sufficient SNR. The same equipment from the previous PIV configuration was used. The two high-speed cameras were equipped with $f = 105\text{-mm}$ macro lenses (Sigma) with aperture settings of $f/4$. Each camera imaged at a digital resolution of $0.28 \text{ mm pixel}^{-1}$ to produce FOVs with dimensions of $226 \times 360 \text{ mm}^2$ in the x and z directions, respectively. The FOVs were stitched together using vector mapping to produce combined dimensions of $380 \times 360 \text{ mm}^2$ in the x and z directions. A combination of cylindrical and spherical lenses was used to generate a 1 mm thick laser sheet. The time-resolved data consisted of 10 sets of 5395 single-frame images recorded at 4 kHz. The SNR of the images was enhanced using the same pre-processing steps discussed above. The images were sequentially cross-correlated using a multi-pass algorithm with a final window size of 32×32 pixels ($9 \times 9 \text{ mm}^2$) with 75 % overlap. The vector fields contained approximately 1 % spurious vectors that were detected and replaced as before.

In the following analysis, the streamwise and spanwise axes, x and z , are normalized using the airfoil chord length (c). The wall-normal axis, y , is normalized using δ_0 , which is the boundary layer thickness measured at $x/c = -0.35$ and is equal to 17.8 mm. All velocity components are normalized with respect to the free-stream velocity U_∞ , which is 11.2 m s^{-1} . The time-averaged velocity components are demonstrated using $\langle \cdot \rangle$. For the analysis of PIV data, an algorithm was developed to identify the detachment location of the TBL based on the most upstream location where the sign of U changes from positive to negative (i.e. flow transitioned from forward to backward flow). The endpoint of the TSB was also detected as the most downstream location, where the sign of U changes from negative to positive (i.e. flow transitioned from backward to forward flow). In detecting the detachment and the endpoints of the TSB, small batches of backward or forward-flow motion with an area smaller than the 10 % of the mean TSB were discarded. This resulted

in greater continuity in the time-series of the detected locations. The algorithm is similar to the procedure applied by Eich & Kähler (2020) for detecting detachment points.

3. Turbulent separation bubble

In this section, we first demonstrate the unsteadiness of the flow using instantaneous visualizations of streamwise velocity and contours of forward-flow probability. The mean velocity fields are then investigated to characterize the time-averaged TSB and to estimate the thickness and Reynolds number of the upstream TBL. Finally, we evaluate contours of the Reynolds stresses to compare the shear layers with those from previous investigations of APG-induced and geometry-induced TSBs.

Figure 2(a) shows an instantaneous sample of the streamwise velocity field in the streamwise–wall-normal plane at the midspan of the wing. The TE is located at $x/c = 0$, and the measurement domain covers a large region of approximately 0.63 m from $x = -0.35c$ upstream of the TE to $x = 0.3c$ downstream of the TE. A sequence of time-resolved velocity fields is also shown in supplementary movie 1 available at <https://doi.org/10.1017/jfm.2022.603>. In figure 2(a), the black line indicates the contour of $U = 0$, which marks the instantaneous boundary of the TSB. The blue region inside the black contour represents the back-flow region with negative U . The TBL separates from the wall at $x/c = -0.16$ as marked with the letter D' (i.e. the detachment point). The TBL remains detached up to the TE while the back flow extends diagonally farther downstream of the TE into the wake region. The most downstream location of the TSB (i.e. the endpoint) is indicated with the letter E' in figure 2(a). The extension of the back-flow region is inclined with respect to the airfoil surface such that it aligns with the high-velocity flow entering the wake from the pressure side of the airfoil. As indicated by the overlaid velocity vectors shown at $x/c = 0.1$, the flow coming from the pressure side has a strong positive V component due to the angle of attack of the airfoil. The velocity field shows the presence of two shear layers on the upper and lower edges of the TSB. The ‘upper’ shear layer forms from the detachment of the TBL on the suction side of the airfoil, while the ‘lower’ shear layer forms from the detachment of the pressure-side boundary layer from the airfoil TE. The latter forms an interface between the high-velocity flow of the pressure side and the extension of the TSB in the wake region. These two shear layers are labelled in figure 2(a) and form a triangular-shaped TSB between D' , E' and the TE. Downstream from the TE, the two shear layers evolve free from the wall and gradually merge into a double-sided shear layer.

The contours of the forward-flow probability, γ , in figure 2(b) show the intermittency of the TSB boundaries. Starting from an upstream location, γ gradually reduces with increasing x/c approximately until the TE. Along a near-wall line of $y/c = 0.003$, γ reaches a minimum value of $\gamma = 0.06$ at $x/c = -0.02$, which is just upstream of the TE. Between $x/c = -0.02$ and the TE, γ rapidly increases to $\gamma = 1$ over a short distance. Scrutiny of the instantaneous visualizations shows occasional forward flows in the small region between $x/c = -0.02$ and the TE. However, since γ reaches a negligible value of 0.06 at a small distance of $0.02c$ upstream of the TE, the TE can be assumed as a fixed corner of the TSB. Downstream of the TE along $y/c = 0$, γ remains equal to 1 due to the high-velocity flow of the pressure side crossing the wake centreline. In contrast, along the diagonal path that is indicated with a dashed line in figure 2(b), γ gradually increases from 0.1 to 0.99 over a distance of approximately $0.1c$. The trailing region of the TSB is therefore highly intermittent as the back-flow region moves back and forth along the dashed line (also see supplementary movie 1). Overall, the results indicate that the TSB features an intermittent detachment on the airfoil surface, an intermittent back-flow region that extends diagonally

Unsteady motions in the turbulent separation bubble

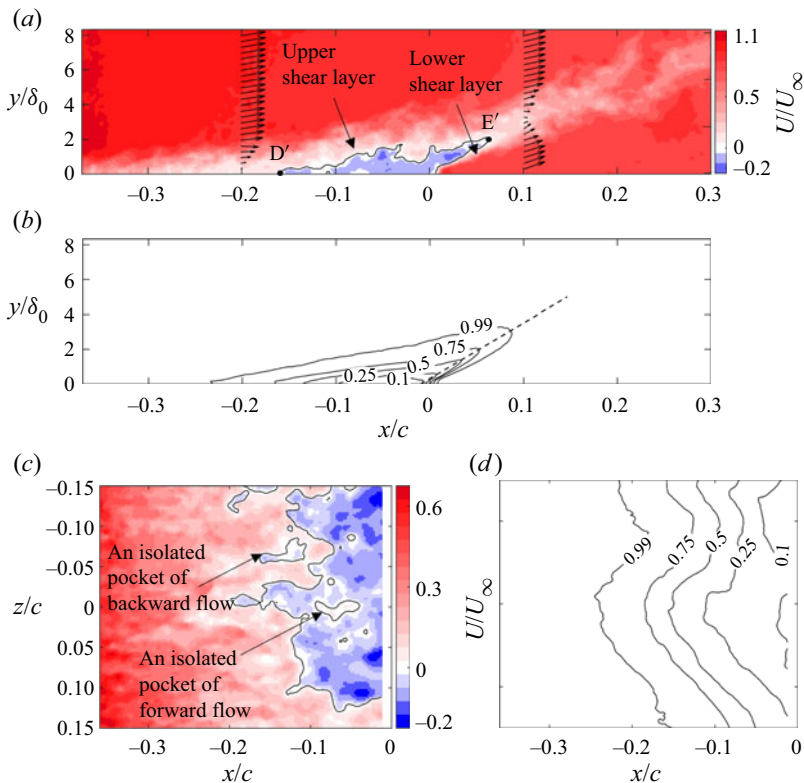


Figure 2. (a) Instantaneous contours of streamwise velocity and (b) contours of γ in the streamwise–wall-normal measurement plane. (c) Instantaneous contours of the streamwise velocity and (d) contours of γ in the streamwise–spanwise plane located at $y/\delta_0 = 0.22$. The detachment and endpoints of the instantaneous TSB are labelled in (a) as points D' and E', respectively.

into the wake region, and a point just upstream of the TE that is approximately fixed. This triangular-shaped TSB is different from the dome-shaped TSBs of Mohammed-Taifour & Weiss (2016), Le Floc'h *et al.* (2020) and Wu *et al.* (2020) that consist of a single shear layer evolving near a wall. For this configuration, the breathing motion is defined as low-frequency variations of the TSB cross-sectional area in the streamwise–wall-normal plane.

An instantaneous streamwise velocity field from the streamwise–spanwise PIV plane is shown in figure 2(c). The TE is located at the most downstream location of this measurement plane at $x/c = 0$. The black line indicates the contour of $U = 0$ which separates the upstream forward flow from the downstream back-flow region and therefore outlines the TSB. This separation line is oriented in the spanwise direction, but it undulates due to the intermittency of the separation location. The undulating pattern of the separation line is attributed to its interaction with the low- and high-speed structures of the incoming TBL (Eich & Kähler 2020; Ma *et al.* 2020). The time instance shown in figure 2(c) also contains a relatively rare event in which the flow stays attached up to the TE at $z/c > 0.13$. There are also a few isolated back-flow regions within the forward-flow region and a few small pockets of forward flow within the separation bubble, as indicated within the figure. To demonstrate these features over time, a sequence of time-resolved velocity fields in the streamwise–spanwise plane is shown in supplementary movie 2.

To statistically investigate the intermittency of the TSB in the streamwise–wall-normal plane, we have plotted the contours of forward-flow probability which are shown in [figure 2\(d\)](#). The iso-contours of γ are mainly oriented in the spanwise direction as the forward-flow probability reduces with increasing x/c . A contour with a low γ of 0.1 is observed just upstream of the TE. It is also observed that the contours have a wavy pattern that undulates in the streamwise direction. The undulation is small relative to the chord length as the maximum oscillation of the $\gamma = 0.99$ contour is approximately $0.1c$. The wavy pattern is due to the presence of three-dimensional (3-D) flow structures that are known as stall cells. These structures commonly form during flow separation on 2-D wings, and each stall cell consists of a saddle point and a pair of foci (Weihs & Katz 1983). Multiple stall cells and asymmetric patterns can form along the wingspan depending on the angle of attack, Reynolds number, airfoil shape and the aspect ratio of the wing (Dell’Orso, Tuna & Amitay 2016; Dell’Orso & Amitay 2018; Wang & Ghaemi 2021). In addition to the stall cells, Wang & Ghaemi (2021) observed that secondary structures are present at the two spanwise ends of the current wing configuration around $z/c = \pm 0.62$, which may contribute to the asymmetry of the wavy pattern of the separation line with respect to the centreline of the wing ($z/c = 0$). However, due to the large span of the wing, these structures are far from the measurement domain and are not expected to affect the TSB dynamics.

Contours of normalized mean streamwise velocity, $\langle U \rangle / U_\infty$, in the streamwise–wall-normal plane are illustrated in [figure 3\(a\)](#). The solid line shows the contour of $\langle U \rangle = 0$, which represents the boundary of the mean TSB. The most upstream point of $\langle U \rangle = 0$ at $x/c = -0.13$ is the mean detachment point, as indicated by the letter D. The end of the mean TSB is specified by the letter E and is located at $(x_E/c, y_E/\delta_0) = (0.03, 1.1)$. The mean length of the separation bubble, l , is defined as the distance between D and E, which is $0.16c$. Similar to the instantaneous TSB, the mean TSB has a triangular shape with its three vertices at D, E and the TE. The TBL over the suction side of the airfoil detaches from the wall and forms the upper shear layer that extends along the DE line. The mean TSB is relatively shallow with an approximate height of $0.02c$, which is attributed to the pre-stall angle of attack of the wing (Wang & Ghaemi 2021). As noted previously, the lower shear layer forms from the separation of the high-speed flow emerging from the pressure side of the airfoil. The upper and lower shear layers are labelled in [figure 3\(a\)](#).

[Figure 3\(b\)](#) shows contours of the normalized wall-normal velocity, $\langle V \rangle / U_\infty$, and the mean flow streamlines in the streamwise–wall-normal plane. The free-stream flow upstream of the measurement domain has a small positive $\langle V \rangle / U_\infty$, mainly due to the downstream blockage caused by the TSB. The wall-normal component then increases with increasing x/c as the flow passes over the TSB. There is a small region of negative $\langle V \rangle / U_\infty$ within the TSB due to the downward motion of the recirculating vortex. A strong upward flow emerges from the pressure side of the airfoil into the wake region. This upward flow pushes the trailing section of the TSB in the positive y direction.

The variation of the boundary layer thickness, δ_{95} , and momentum thickness, θ , of the incoming TBL with respect to x/c is demonstrated using the left-side axis of [figure 3\(c\)](#). The streamwise extent of the reported δ_{95} and θ in this figure is limited to the region where the TBL stays attached to the wall. Due to the wall-normal limit of the measurement domain, the boundary layer thickness has been obtained based on the y location where $\langle U \rangle = 0.95U_\infty$, and the integration of the velocity profiles for calculating θ is also carried out up to the same location where $\langle U \rangle = 0.95U_\infty$. [Figure 3\(a\)](#) shows that both δ_{95} and θ gradually increase with respect to x/c until $x/c = -0.22$ where the change in δ_{95} and θ suddenly increases. The sudden increase is attributed to the instantaneous presence of back

Unsteady motions in the turbulent separation bubble

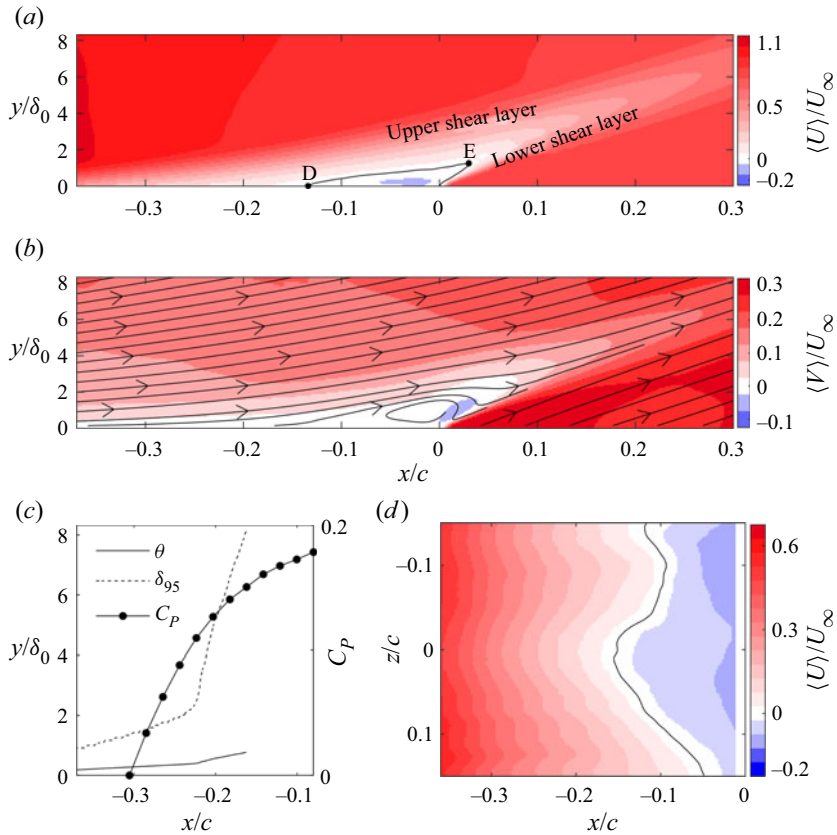


Figure 3. (a) Contours of $\langle U \rangle / U_\infty$ in the streamwise–wall-normal plane revealing the triangular-shaped TSB. (b) Contours of $\langle V \rangle / U_\infty$ in the streamwise–wall-normal plane with an overlay of mean flow streamlines. (c) The variation of boundary layer thickness, momentum thickness and the pressure coefficient with streamwise distance. (d) Contours of $\langle U \rangle / U_\infty$ in the streamwise–spanwise plane. In (a) and (d), the black line shows the contour of $\langle U \rangle = 0$. The detachment and endpoints of the time-averaged TSB are labelled in (a) as points D and E, respectively.

flow (γ becoming smaller than 1) as can be seen in figure 2(b). The value of Re_θ , which is calculated based on U_∞ and θ at an upstream location of $x/c = -0.35$, is approximately 2800. This Re_θ is larger than the Re_θ of 490 considered in the DNS of Wu *et al.* (2020) but smaller than the Re_θ of 5000 considered by Weiss *et al.* (2015). The friction Reynolds number, Re_τ , defined using friction velocity and boundary layer thickness, is approximately equal to 900. This value is estimated here using the $Re_\tau = 1.13 \times Re_\theta^{0.843}$ equation proposed by Schlatter & Örlü (2010).

The right-side axis of figure 3(a) also shows the variation of the static pressure coefficient, C_p , measured along the midspan of the wing from $x/c = -0.31$ to -0.08 . The results reveal the presence of an APG with a larger increase in C_p upstream of the TSB from $x/c = -0.31$ to approximately $x/c = -0.2$. This is followed by a slower increase in C_p from $x/c = -0.2$ to -0.08 , which overlaps with the mean TSB. The largest C_p observed here is approximately half of the maximum C_p reported in the experiments of Weiss *et al.* (2015) and Le Floc’h *et al.* (2020) and the simulations of Wu *et al.* (2020).

The contours of $\langle U \rangle / U_\infty$ in the streamwise–spanwise plane are shown in figure 3(d). The separation point along the midspan ($z/c = 0$) is at $x/c = -0.15$, which is slightly

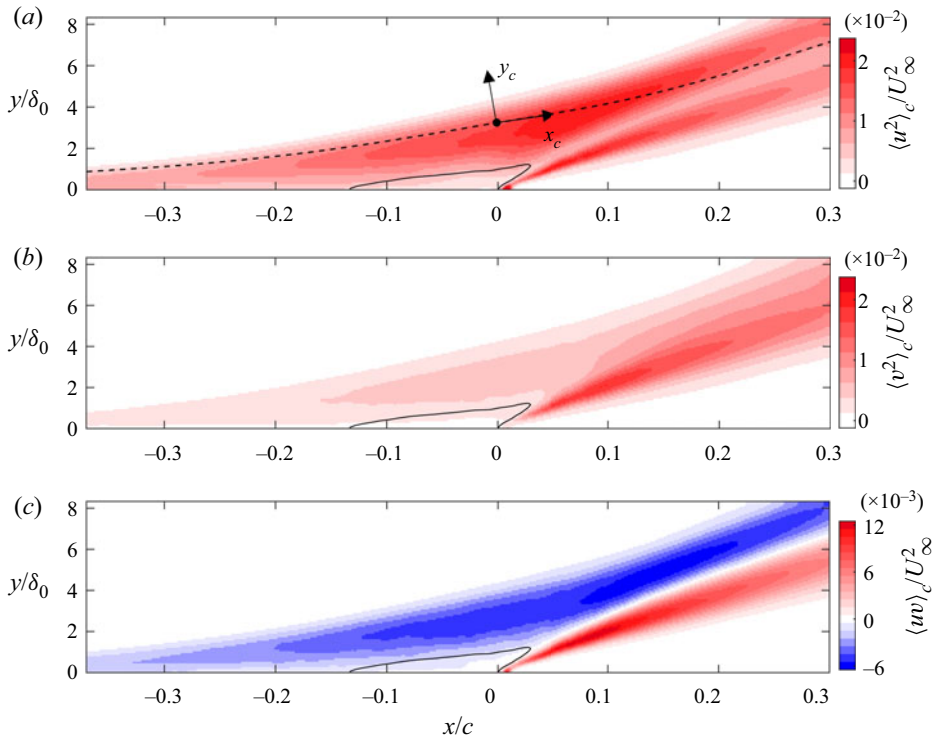


Figure 4. The contours of (a) $\langle u^2 \rangle_c$, (b) $\langle v^2 \rangle_c$ and (c) $\langle uv \rangle_c$, normalized by U_∞^2 . The velocity components are computed in the curvilinear x_c – y_c coordinate system shown in (a). The contour line shows the boundary of the mean TSB based on $\langle U \rangle = 0$.

downstream of the point D detected in figure 3(a). This small shift is because the wall-parallel measurement plane is at approximately $y/\delta_0 = 0.22$ while the first data point in the streamwise–wall-normal PIV plane is at $y/\delta_0 = 0.17$. The contours of mean velocity exhibit a wavy separation line, which is similar to the pattern of the γ contours in figure 2(d). As was discussed previously, the wavy pattern and its asymmetry are associated with stall cells and secondary structures formed along the wingspan (Wang & Ghaemi 2021).

The Reynolds stresses are calculated with respect to a curvilinear coordinate system with x_c and y_c axes based on a streamline that approximately follows the loci of maximum spanwise vorticity along the upper shear layer. The path of the curvilinear coordinate system is shown with a dashed line in figure 4(a). The x_c axis remains tangent to the line while its positive direction is in the flow direction. The y_c axis is perpendicular to x_c and is positive in the counterclockwise direction with respect to the positive x_c axis. The parameters calculated in this curvilinear coordinate system are shown with subscript c . The conversion of the Reynolds stresses from the fixed x – y coordinate system to this curvilinear coordinate system is performed following Wu & Piomelli (2018) and Fang & Tachie (2020). Inspection of the Reynolds stresses in the x – y and x_c – y_c coordinates shows that the magnitudes are different while the spatial pattern of the Reynolds stresses remains similar.

The normalized contours of streamwise Reynolds stress, $\langle u^2 \rangle_c$, in figure 4(a) exhibit two high-intensity zones that correspond to the upper and lower shear layers. The upper shear layer is wider and has a slightly higher peak intensity. Along the upper shear layer, the

magnitude of $\langle u^2 \rangle_c$ initially rises with increasing x/c and reaches its maximum downstream of the TE at approximately $x/c = 0.1$. Farther downstream, $\langle u^2 \rangle_c$ gradually decreases as the upper shear layer progresses into the wake region. This trend is similar to the distribution of streamwise Reynolds stress shown in the APG-induced TSBs of Mohammed-Taifour & Weiss (2016), Le Floc'h *et al.* (2020) and Mohammed-Taifour & Weiss (2021). In these investigations, the streamwise Reynolds stresses demonstrated a single peak within the shear layer, which was close to the detachment point. The DNS of Wu *et al.* (2020) also shows a single peak near the detachment location when they forced the shear layer to reattach by imposing an FPG. In contrast, when Wu *et al.* (2020) did not apply a FPG, a strong second peak appeared close to the reattachment region. The shear layer in the DNS of Na & Moin (1998) also shows two local peaks of streamwise Reynolds stress; the first one was close to the detachment point and the second one was in the downstream part of the TSB. In both Wu *et al.* (2020) and Na & Moin (1998), the second peak potentially forms due to stronger interactions between the shear-layer vortices and the wall during the gradual reattachment process. Such an interaction is not present for the TE separation of the current investigation as the shear layer departs from the airfoil surface and oscillates freely in the wake region. In addition, the current TSB has a strong lower shear layer with two peaks: a small intense region of $\langle u^2 \rangle_c$ near the TE and a second peak farther downstream at approximately $x/c = 0.05$.

Normalized contours of $\langle v^2 \rangle_c$ are shown in figure 4(b), where the upper shear layer has a significantly weaker magnitude relative to the lower shear layer. Our analysis indicates that the difference is not due to the alignment of the curvilinear coordinate system with the upper shear, as the magnitude of $\langle v^2 \rangle_c$ in the lower shear layer is greater than that of the upper shear layer even if the curvilinear coordinate system is aligned with the trajectory of the lower shear. The greater $\langle v^2 \rangle_c$ of the lower shear layer is associated with the greater velocity gradient across the lower shear layer, as can be seen in figure 3(a). This results in the roll-up of stronger spanwise vortices. The intense wall-normal velocity fluctuations of the lower shear also result in stronger Reynolds shear stresses as shown in figure 4(c). The high $\langle uv \rangle_c$ region of the lower shear layer is narrower and more concentrated relative to the upper shear layer. The normalized $\langle uv \rangle_c$ in the lower shear layer reaches 0.012, while it only reaches -0.003 along the upper shear layer. As expected, both shear layers contribute to the production of turbulence; the opposite $\langle uv \rangle_c$ signs cancel with the opposite signs of mean velocity gradient, $d\langle U \rangle_c/dy_c$, for the two shear layers. The Reynolds stress distributions also show that the two shear layers do not fully merge within the measurement domain as they maintain separate regions of strong Reynolds stresses. However, the lower shear layer dominates the upper shear layer in terms of wall-normal and shear Reynolds stresses. This contrasts with the previous investigations of TSBs on flat plates in which the Reynolds stresses are concentrated in the single shear layer that forms above the TSB.

The normalized intensity of Reynolds stresses in the current TSB can be compared with those of turbulent plane mixing layers. The $\langle u^2 \rangle_c/U_\infty^2$ peak of the upper and lower shear layers in figure 4(a) reach 0.02, which is similar to the 0.03 peak observed in Forliti, Tang & Strykowski (2005) and Loucks & Wallace (2012) for plane shear layers. In contrast, only the $\langle v^2 \rangle_c/U_\infty^2$ peak of the lower shear layer is similar to the $\langle v^2 \rangle_c/U_\infty^2$ peak of 0.02 observed in Forliti *et al.* (2005) and Loucks & Wallace (2012). A similar observation is made for Reynolds shear stress. The $\langle uv \rangle_c/U_\infty^2$ peak of the lower shear layer in figure 4(c) is similar to the 0.01 peak reported in Loucks & Wallace (2012), while the peak value of the upper shear layer is an order of magnitude smaller. Therefore, the intensity of Reynolds

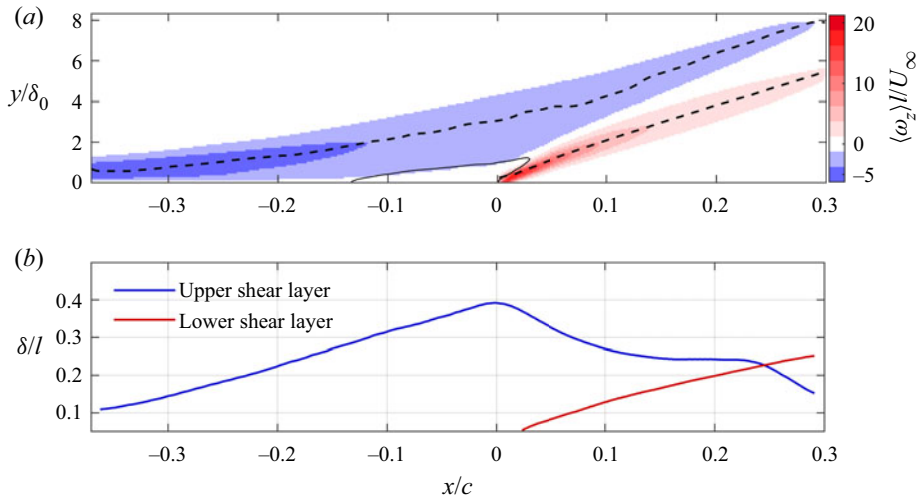


Figure 5. (a) Contour of $\langle \omega_z \rangle$ normalized by U_∞/l . The black dashed lines follow the location of peak vorticity, $\langle \omega_z \rangle_{peak}$, along the upper and lower shear layers. (b) The variation of vorticity thickness, δ , for the upper and lower shear layers with respect to x/c .

stresses in lower shear layer of the TSB resembles those of plane shear layers, while the upper shear layer demonstrates smaller values of wall-normal and shear Reynolds stresses.

To characterize the thickness of the shear layers, the distribution of the normalized mean spanwise vorticity, $\langle \omega_z \rangle/l/U_\infty$, is shown in figure 5(a). The trajectories of the maximum vorticity along each shear layer are also plotted as black dashed lines. The upper shear layer has a wide region of negative $\langle \omega_z \rangle$, while the lower shear layer has a thin zone of positive $\langle \omega_z \rangle$. For both shear layers, the $\langle \omega_z \rangle$ magnitude gradually reduces in the flow direction. The shear-layer thickness δ is estimated as the wall-normal extent of the region where $|\langle \omega_z \rangle / \langle \omega_z \rangle_{peak}| > 1/e$. Here, $\langle \omega_z \rangle_{peak}$ is the local maximum vorticity and e is the exponential constant. The estimated δ has been normalized using l and is shown in figure 5(b). The results show that the thickness of the upper shear layer initially increases with increasing x/c until the TE, at which point the thickness of the layer reduces, potentially due to the appearance of the lower shear layer. Within $0.16 < x/c < 0.22$, the thickness of the upper shear stays relatively constant at $\delta/l \approx 0.24$, and then reduces again close to the end of the measurement domain. In contrast, the thickness of the lower shear layer continuously increases within the measurement domain, and even surpasses the thickness of the upper shear layer at $x/c = 0.24$.

4. Unsteady motions

To characterize the frequency and energy of flow unsteadiness, the pre-multiplied power spectral density (PSD) of streamwise velocity fluctuations (u) along $y/\delta_0 = 1.0$ is presented in figure 6(a). The PSD was calculated by dividing each of the 15 datasets into 3 segments with 50% overlap. This resulted in 45 periodograms, each $44l/U_\infty$ long, which were normalized using the square of the free-stream velocity and then multiplied by f . Note again that St_l is defined as fl/U_∞ where the length scale, l , is equal to the length of the upper edge of the mean TSB ($0.16c$). The pre-multiplied PSD contours show strong unsteadiness in the upstream TBL, inside the TSB, and across the lower shear layer as labelled in figure 6(a). In the upstream TBL, the energetic flow motions have a high St_l of

Unsteady motions in the turbulent separation bubble

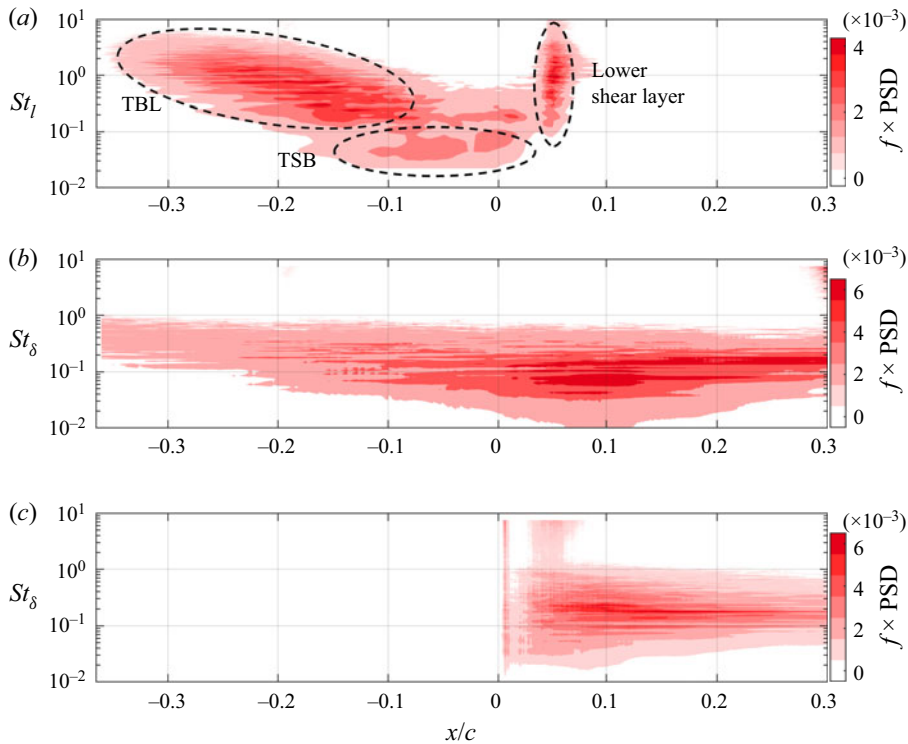


Figure 6. Contours of the pre-multiplied PSD of u along (a) $y/\delta_0 = 1.0$, (b) the upper shear layer and (c) the lower shear layer. Note that $St_l = 4.2 \times St_\delta$.

approximately 4, which gradually reduces to 0.1 with increasing x/c . The reduction in the St_l of the TBL fluctuations is attributed to the effect of the APG on the low- and high-speed structures (Skote & Henningson 2002; Lee & Sung 2009; Eich & Kähler 2020).

A zone of energetic motions with small St_l is observed in the range $-0.15 < x/c < +0.02$, which overlaps with the streamwise location of the TSB where forward-flow probability is relatively small. According to figure 2(b), γ varies from 0.5 to 0.1 within this high-energy zone. The maximum energy of these motions is centred at St_l of 0.06 while some of the fluctuations occur at smaller St_l of 0.03. These frequencies are similar to the $St_l = 0.03$ reported for the breathing motion by Weiss *et al.* (2015). The current investigation indicates that energetic velocity fluctuations with small $St_l = 0.03$ are present in an APG-induced TSB. The observation of low St_l breathing motion by Weiss *et al.* (2015) was based on wall-pressure measurements, which can be the result of flow motions throughout the whole flow field. The PSD of streamwise velocity by Wu *et al.* (2020) also does not indicate the present of velocity fluctuations at such a low frequency, potentially because their spectrum was limited to $St_l > 0.2$ and the streamwise velocity was averaged over the spanwise direction. We will further investigate these low St_l motions to characterize their spatial structure and indicate whether they are related to the breathing motion.

Figure 6(a) also reveals a zone of energetic flow motions with St_l varying from 0.1 to 10 at $x/c = 0.04$. This location is downstream of the TE and corresponds to the intersection of the lower shear layer with $y/\delta_0 = 1.0$. The wide St_l range at this location is a result of the spatial displacement of the shear layer as seen by a fixed grid point of the PIV FOV. As the shear layer oscillates in space, the turbulent shear layer and the free-stream flow

intermittently occupy the PIV grid point, and therefore the pre-multiplied PSD spreads over a broad range of St_l from 0.1 to 10. To address this issue, the pre-multiplied PSDs of u have been computed along the upper and lower shear layers and are presented in figures 6(b) and 6(c), respectively. The trajectories along which the pre-multiplied PSDs were computed are the same as those shown with dashed lines in figure 5(a). Moreover, to allow for comparison of the present results with previous characterizations of shear layers, the frequency was normalized as $St_\delta = f\delta/U_\infty$. Here, δ is the thickness of the upper shear layer at $x/c = 0.2$, which is equal to $0.24l$ based on figure 5. The contours of figure 6(b) show that the energy of the fluctuations increases with increasing x/c along the upper shear layer. The strongest oscillations are observed close to the TE, at approximately $x/c = 0.1$, with a St_δ of 0.05 to 0.2 (equivalent to St_l of 0.2 to 0.8). With increasing x/c , the oscillations converge to St_δ of 0.15 (St_l of 0.4). The results for the lower shear layer in figure 6(c) show energetic motions at St_δ of 0.1 to 0.2 (St_l of 0.4 to 0.8). The value of St_δ of the flow oscillations along both shear layers is similar to the Strouhal number of vortex shedding reported in previous experimental investigations (Maull & Young 1973; Sigurdson 1995) and the Strouhal number of the most amplified frequencies predicted by the linear stability theory for shear layers (Monkewitz & Huerre 1982). Therefore, both shear layers are subject to Kelvin–Helmholtz instabilities, which result in the roll-up of the shear layer and vortex shedding.

5. Temporal and spatial scales

The temporal evolution of spanwise profiles of u/U_∞ is shown in figure 7 for three x/c locations of -0.25 (within the upstream TBL), -0.15 (close to the mean separation point) and -0.05 (within the TSB). The vertical axis of the figure is the spanwise axis of the flow, z/c , while the horizontal axis is the normalized time, t/T . Here, T is a time scale defined as l/U_∞ . All the data correspond to $y/\delta_0 = 0.22$, which is the wall-normal location of the streamwise–spanwise PIV plane. The flow pattern at $x/c = -0.25$ includes streamwise regions of low- and high-speed flows. The structures meander in the spanwise direction and they have a spanwise spacing of approximately $0.04c$, which is equal to $1.1\delta_{95}$ (based on the local thickness of the TBL at $x/c = -0.25$). This spanwise spacing is similar to the spanwise spacing of $\sim 1\delta_{95}$ reported by Ganapathisubramani *et al.* (2005) for large-scale motions at $y/\delta_{95} = 0.5$ in a TBL with $Re_\tau = 1100$. Therefore, the wall-normal location of the measurement plane ($y/\delta_0 = 0.22$) and the spanwise spacing of the structures seen at $x/c = -0.25$ suggest that the pattern corresponds to the large-scale motions (LSM) and the very-large-scale motions of the outer layer (Balakumar & Adrian 2007; Hutchins & Marusic 2007).

At $x/c = -0.15$ and -0.05 in figure 7, which correspond to upstream of the mean TSB and within the TSB, the flow pattern consists of large zones of positive and negative velocity fluctuations. These zones have a large spatio-temporal coherence; they are several times wider than those observed at $x/c = -0.25$ and they appear longer along the time axis. The latter suggests that they have a slower advection velocity or a longer streamwise length. The large zones at $x/c = -0.15$ and -0.05 resemble the highly elongated streamwise structures that Wu *et al.* (2020) observed in the low-frequency modes of their DMD analysis. They attributed the structures to Görtler vortices generated by the curvature of the streamlines as the flow passes over the separated region. The zones also resemble the large Görtler structures shown by You, Buchta & Zaki (2021) in the DNS of a TBL over a concave wall.

To further investigate the spatial and temporal scales of the structures, the fluctuating streamwise velocity along the x -axis is plotted versus time in figure 8. The data correspond

Unsteady motions in the turbulent separation bubble

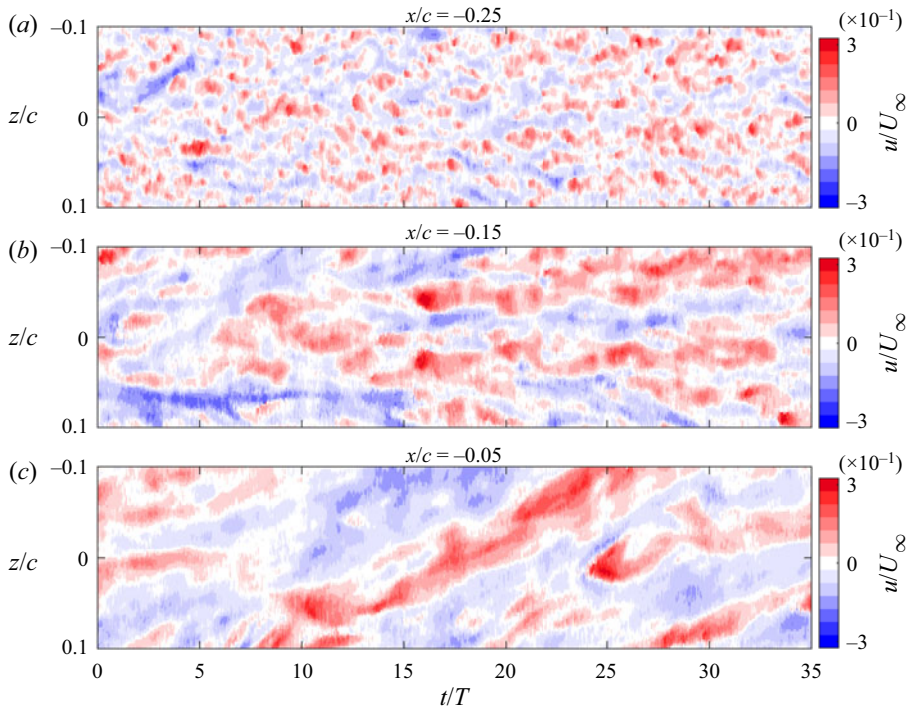


Figure 7. Instantaneous visualization of spanwise profiles of u/U_∞ as they evolve in time at three streamwise locations of $x/c = -0.25$, -0.15 and -0.05 .

to a streamwise profile of u/U_∞ at the midspan of the wing ($z/c = 0$) and are extracted from the streamwise–spanwise PIV plane. To illustrate structures with both short and long temporal scales, [figure 8\(a\)](#) shows a shorter duration of $20T$ while [figure 8\(b\)](#) shows a longer duration of $98T$. The instantaneous separation line, which is the location of $U = 0$, is also shown with a solid black line. A pattern of inclined low- and high-speed structures is seen upstream of the separation region at approximately $x/c < -0.2$ within [figure 8\(a\)](#). Each stripe shows the advection of a low- or a high-velocity structure in the x – t domain. Since the large-scale structures of TBLs meander in the z -direction, the length of the stripes visible in [figure 8](#) does not reveal their full streamwise extent or lifetime. However, the inclination/slope of each stripe, i.e. dx/dt of the lines tangent to the stripes, indicates their advection speed. For example, the slope of the dashed line seen at $t/T \approx 2$ in [figure 8\(a\)](#) indicates that the high-speed structure tangent to this line moves downstream at a speed of $0.4U_\infty$. As the structures approach the separation line, they become wider and their slopes reduce, thus indicating a slower advection speed. The widening is pronounced for the high-speed structures in the region immediately upstream of the instantaneous separation line. The slower advection speed is seen by the gradual departure of the high-speed structure at $t/T \approx 2$ from its corresponding dashed line. In addition, the horizontal spacing between the adjacent structures along the t/T axis represents their frequency. The closely packed structures at $x/c < -0.2$ appear to alternate in periods as short as $0.5T$, which is equivalent to $St_l = 2$. Therefore, the high-frequency oscillations that were observed within the upstream TBL of [figure 6\(a\)](#) are indeed associated with the TBL structures.

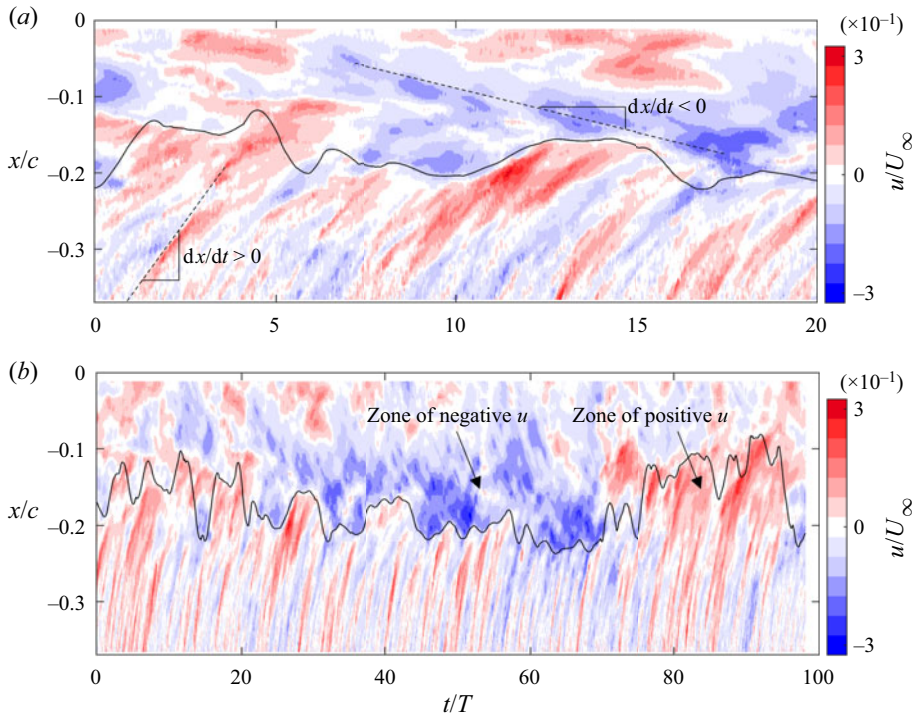


Figure 8. The temporal evolution of streamwise profiles of u/U_∞ over (a) a short duration of $20T$ and (b) a longer duration of $98T$. The data correspond to the midspan of the wing ($z/c = 0$) from the streamwise–spanwise PIV plane at $y/\delta_0 = 0.22$.

Once the flow reaches the separation region at approximately $x/c = -0.2$ of figure 8(a), the large zones of positive and negative velocity fluctuation emerge. These large zones correspond to the motions within the TSB (under the separated shear layer) along the $y/\delta_0 = 0.22$ plane. They extend along the time axis and occasionally appear to linger at a fixed location due to their lower advection speeds. As seen from the negative slope of the dashed line drawn at $t/T \approx 7$ in figure 8(a), some of the zones with negative u appear to slowly advect in the upstream direction, i.e. a back-flow motion within the TSB. The positive and negative zones of the TSB alternate slowly over long periods reaching up to $50T$ as seen in the longer sequence of figure 8(b). This duration is equivalent to $St_l = 0.02$, which is similar to the low St_l motions observed within the TSB in figure 6(a). It is also observed that the separation line in figure 8(b) closely follows the pattern of these large zones. At $t/T \approx 50$ a negative zone results in the separation front moving in the upstream direction, while at $t/T \approx 90$ a positive zone results in the separation front moving downstream.

The present results indicate that the TSB is formed from large zones featuring positive and negative streamwise velocity fluctuations. When compared with the low- and high-speed structures of the upstream TBL, these TSB structures are several times wider and their time scale is approximately two orders of magnitude greater. These low- and high-speed zones result in the energetic, low-frequency region labelled as TSB in the pre-multiplied PSD of figure 6(a).

In figure 9, the spatial and temporal scales of the turbulent structures are quantified using results extracted from two-point correlations of the streamwise velocity fluctuations.

Unsteady motions in the turbulent separation bubble

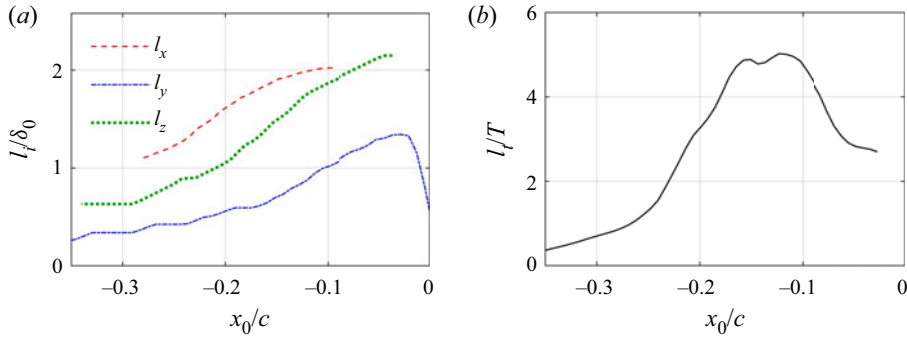


Figure 9. The (a) spatial and (b) temporal scales of the motions estimated based on two-point correlations of the streamwise velocity fluctuations. The spatial scales, l_i , are normalized using δ_0 , and the temporal scale is normalized using T , defined as l/U_∞ .

The reference point for these correlations was placed at a spatial location of (x_0, y_0, z_0) and at an arbitrary reference time, t_0 . The correlation coefficient, R_{uu} , was calculated according to

$$R_{uu}(\Delta x, \Delta y, \Delta z, \Delta t) = \frac{\langle u(x_0, y_0, z_0, t_0)u(x_0 + \Delta x, y_0 + \Delta y, z_0 + \Delta z, t_0 + \Delta t) \rangle}{\sqrt{\langle u^2(x_0, y_0, z_0, t_0) \rangle} \sqrt{\langle u^2(x_0 + \Delta x, y_0 + \Delta y, z_0 + \Delta z, t_0 + \Delta t) \rangle}}. \quad (5.1)$$

In this equation, Δx , Δy , Δz and Δt indicate the spatial and temporal offsets of the traversed data point with respect to the reference point. Each offset was applied separately, e.g. when Δx was varied, Δy , Δz and Δt were kept constant at zero. The streamwise location of the reference point was varied within $-0.35 < x_0/c < 0$ when Δy , Δz and Δt were applied. A smaller streamwise extent of $-0.28 < x_0/c < -0.11$ was used while varying Δx to ensure that $x_0 \pm \Delta x$ remains within the measurement domain. To improve the statistical convergence, the correlation functions were averaged along the spanwise direction of the measurement domain where possible. Once the correlation functions were obtained, the length and time scales of the structures were determined as the point at which $R_{uu} = e^{-1}$. The estimated streamwise, wall-normal, and spanwise length scales are denoted by l_x , l_y and l_z , and the temporal scale is denoted by l_t . The wall-normal scale, l_y , was obtained from the streamwise–wall-normal PIV plane, while l_x , l_z and l_t were obtained from the streamwise–spanwise PIV plane. For consistency, the wall-normal location of the reference points in the streamwise–wall-normal PIV plane was selected as $y_0 = 0.22\delta_0$, which is the same location as the streamwise–spanwise plane.

In figure 9(a), all length scales can be seen to increase with increasing x_0/c . The largest rate of increase in l_x is seen at approximately $x_0/c = -0.24$, which overlaps with the start of the intermittency boundary of the TSB (the $\gamma = 0.99$ contour, figure 2b). Farther downstream at $x_0/c = -0.1$, the rate of increase in l_x is small as its curve appears to approach an asymptotic value. This asymptotic value is approximately twice the value of l_x at $x_0/c = -0.28$, which suggests that the structures become longer by a factor of 2. However, it is important to note that the estimated length scale does not consider the spanwise meandering of the associated structures and therefore l_x does not represent their true length. A similar trend is also observed for l_z , which indicates that the length scale increases by a factor of three with increasing x_0/c . For l_y , we observe a sharp reduction just upstream of the TE at $x_0/c = -0.02$. Inspection of the instantaneous velocity fields shows that this reduction is due to the frequent presence of forward flow in this region,

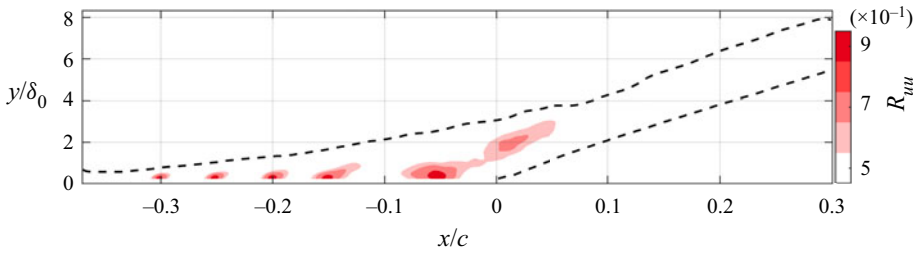


Figure 10. The correlation functions for five reference points located at $y_0/\delta_0 = 0.22$ and $x_0/c = -0.3, -0.25, -0.2, -0.15$ and -0.05 . The most downstream correlation function shows a double-peak pattern.

which is indicated by the rapid increase in γ just upstream of the TE shown in [figure 2\(b\)](#). Overall, the larger length scales of the structures within the TSB are consistent with the visualizations of [figures 7](#) and [8](#). The estimated time scale, l_t , in [figure 9\(b\)](#) also increases with increasing x_0/c until approximately $x_0/c = -0.15$, where l_t can be seen to reach a maximum value. The large time scale at this location agrees with the low St_l motions observed within the TSB in [figure 6\(a\)](#). Farther downstream, l_t decreases and reaches a smaller value of approximately 2.7. This analysis using two-point correlations statistically confirms the TSB zones have a greater spatial and temporal scale with respect to the largest structures of the upstream TBL.

To identify the source of the large low- and high-speed zones of the TSB, we evaluate the formation of Görtler vortices (Görtler 1954) following the procedure applied by Wu *et al.* (2020). The Görtler number, G_T , is calculated using the local radius of curvature of several streamlines that closely pass over the mean TSB. For calculating G_T , an effective eddy viscosity is also calculated using the streamwise–wall-normal component of Reynolds shear stress. The results show that G_T value reaches the 0.3 criterion that is required for the formation of Görtler vortices at approximately $x/c = -0.22$ and then rapidly increases beyond this limit until the mean separation point is reached. In addition, δ_{95}/R also serves as a criterion for predicting the presence of Görtler vortices (Floryan 1991). The δ_{95}/R value reaches the proposed limit of 0.01 at approximately $x/c = -0.25$ and then rapidly increases beyond this limit to values of the order of 0.1 at $x/c = -0.1$. Therefore, both G_T and δ_{95}/R suggest that Görtler vortices can form upstream of the current TSB. We conjecture that the large low- and high-speed zones that are observed at $x/c = -0.15$ and -0.05 of [figure 7](#) and the downstream region of [figure 8](#) correspond to the footprint of the Görtler vortices.

The R_{uuu} contours for simultaneous streamwise and wall-normal shifts (Δx and Δy) are shown in [figure 10](#). Five reference locations at $y_0/\delta_0 = 0.22$ and $x_0/c = -0.3, -0.25, -0.2, -0.15$ and -0.05 were selected from the streamwise–wall-normal PIV plane. The centrelines of the upper and lower shear layers (from [figure 5a](#)) are also shown in [figure 10](#) using dashed lines. As expected from [figure 9](#), the correlation function becomes larger in the streamwise and wall-normal directions with increasing x_0/c . The correlation patterns are also slightly inclined in the position x direction. Interestingly, the last correlation function, which features a reference at $(x_0, y_0) = (-0.05c, 0.22\delta_0)$, shows a double-peak pattern with the second peak located between the upper and lower shear layer at $(x/c, y/\delta_0) = (0.02, 2.0)$. This correlation pattern indicates that the large positive and negative zones of the TSB correlate with the velocity fluctuations generated between the two shear layers by the vortex shedding process.

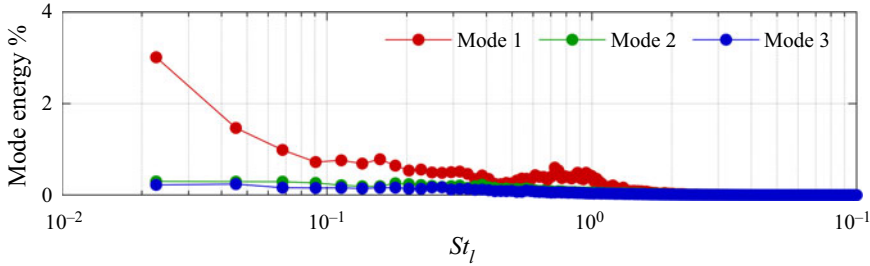


Figure 11. The energy spectra of the first three SPOD modes calculated from the streamwise–wall-normal velocity fields.

6. Energetic motions

In this section, SPOD of the velocity fields, based on the algorithm described by Towne, Schmidt & Colonius (2018), is used to identify the frequency and spatial pattern of the energetic motions. This algorithm decomposes the Fourier transform of the velocity fields into spatial modes, $\Phi_i(\mathbf{x}, f)$ and expansion coefficients, $\mathbf{a}_i(f)$. Here, the index i denotes the mode number, and \mathbf{x} is a vector indicating the spatial location.

Figure 11 shows the energy associated with the first three SPOD modes. These SPOD modes have been obtained from both components of the streamwise–wall-normal velocity fields using 15 planar PIV datasets. Each dataset is approximately 1.21 s long and is divided into three blocks with 50% overlap for SPOD calculations. As expected, the first mode captures the highest percentage of the energy, while the second and third modes have a negligible energy across the frequency spectrum. The separation in the energy of the first and second mode is relatively large at $St_l < 0.1$, which indicates a low-rank behaviour (Schmidt *et al.* 2018). The first mode shows the highest energy at the lowest resolved St_l of 0.02, which is similar to the St_l of breathing motion reported by Weiss *et al.* (2015) and Mohammed-Taifour & Weiss (2016). The first mode also exhibits smaller local peaks at approximately $St_l = 0.16$ and 0.72 . The St_l of these peaks is close to the vortex shedding frequency, which is approximately at $St_l = 0.2$ to 0.8 according to figure 6.

The spatial patterns of the first SPOD mode at $St_l = 0.02$, 0.16 and 0.72 from the streamwise–wall-normal plane are shown in figure 12. In addition, a reduced-order model (ROM) of the flow field, U_{ROM} , has been constructed using the mean velocity field and the selected mode following

$$U_{ROM,i} = U + \Phi_{i(x,f_0)} e^{2\pi i f_0 t}. \tag{6.1}$$

Here, t is time and f_0 is the frequency of the selected SPOD mode used for reconstructing the ROM. The forward-flow probability, γ , for the ROMs constructed from each spatial mode at the selected f_0 was then computed and is shown using the contour lines in figure 12. The spatial pattern of the first mode at St_l of 0.02 consists of a large, inclined structure that is approximately aligned with the upper shear layer. The γ contours of this first mode show that it is associated with the large-scale expansion and contraction of the TSB. These contours are also similar to those of the forward-flow probability previously observed in figure 2(b), which shows that this spatial pattern captures the dominant large-scale unsteadiness within the streamwise–wall-normal plane. The small St_l of this SPOD mode and the fact that this mode is the main contributor to the intermittency of the TSB suggest that it is associated with the breathing motion of the TSB. As noted previously, in the context of TE separation, the breathing motion is defined as

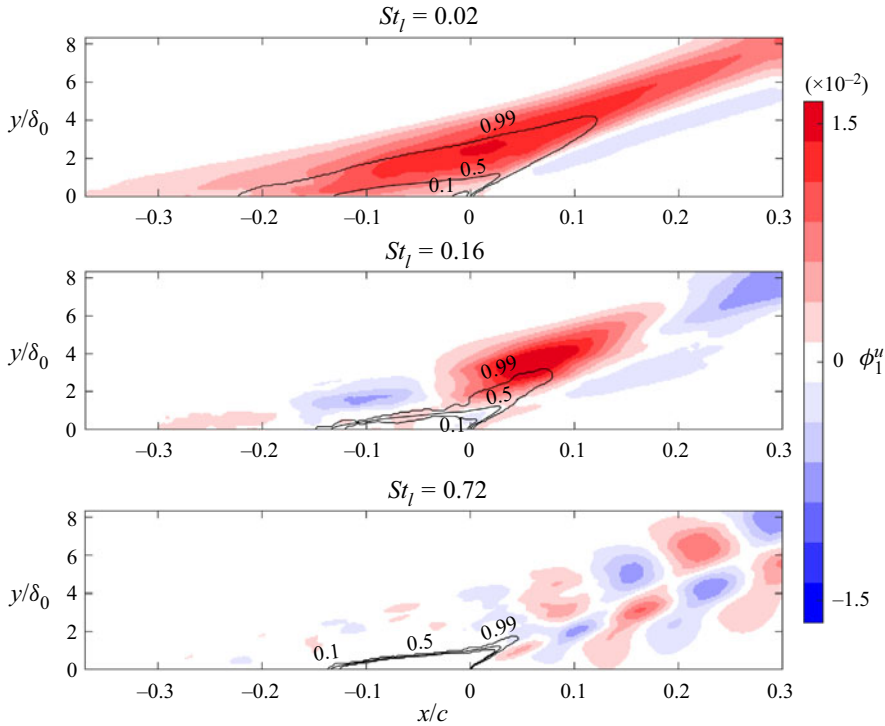


Figure 12. The spatial structures of the first SPOD mode from the streamwise–wall-normal plane at $St_l = 0.02$, 0.16 and 0.72. The contour lines represent the forward-flow probability obtained from the ROM following (6.1).

low-frequency variations of the TSB cross-section. This SPOD mode is consistent with the proper orthogonal decomposition (POD) analysis of Mohammed-Taifour & Weiss (2016), which showed that the first POD mode in the streamwise–wall-normal plane is associated with the breathing motion. The second and third spatial patterns at $St_l = 0.16$ and 0.72 in figure 12 feature smaller structures that develop along the shear layers. The alternating spatial patterns, and their large St_l suggest that they capture the vortex shedding process of the shear layers. The intermittency contours in figure 12 indicate that the spatial pattern at St_l of 0.16 produce a considerable expansion/contraction of the TSB near the TE, while the spatial pattern at St_l of 0.72 does not result in a significant expansion or contraction of the TSB.

The three most energetic SPOD modes obtained using u and w from 10 datasets of the streamwise–spanwise PIV are shown in figure 13. Each dataset is approximately 1.35 seconds and is divided into three blocks with 50% overlap (30 blocks in total). For all three modes, the low-frequency oscillations have a higher energy, with the maximum energy seen at the smallest St_l of 0.02. The energy of the modes quickly reduces with increasing St_l as most of the energy is at $0.02 < St_l < 0.1$. In contrast to the SPOD modes of the streamwise–wall-normal velocity fields, there is no secondary peak at higher St_l . The small St_l of the energetic range frequency band suggests that the spatial modes do not attribute to LSM of the incoming TBL with $0.1 < St_l < 5$, or the vortex shedding process with $St_l = 0.4$.

The spatial patterns of the first SPOD mode at four St_l values of 0.02, 0.04, 0.06 and 0.08 are shown in figure 14. The forward-flow probability from the associated ROMs is also shown using contour lines. At $St_l = 0.02$ and 0.04, a single large-scale structure

Unsteady motions in the turbulent separation bubble

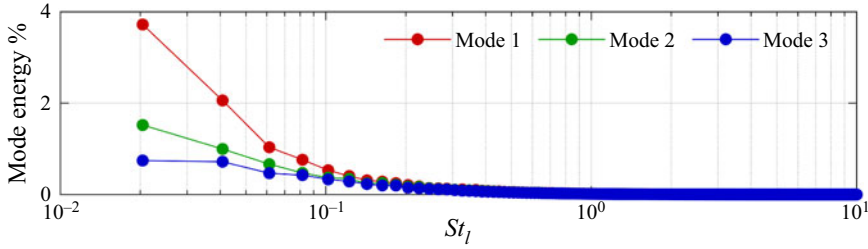


Figure 13. The energy spectra of the first three SPOD modes obtained from the streamwise–spanwise velocity fields.

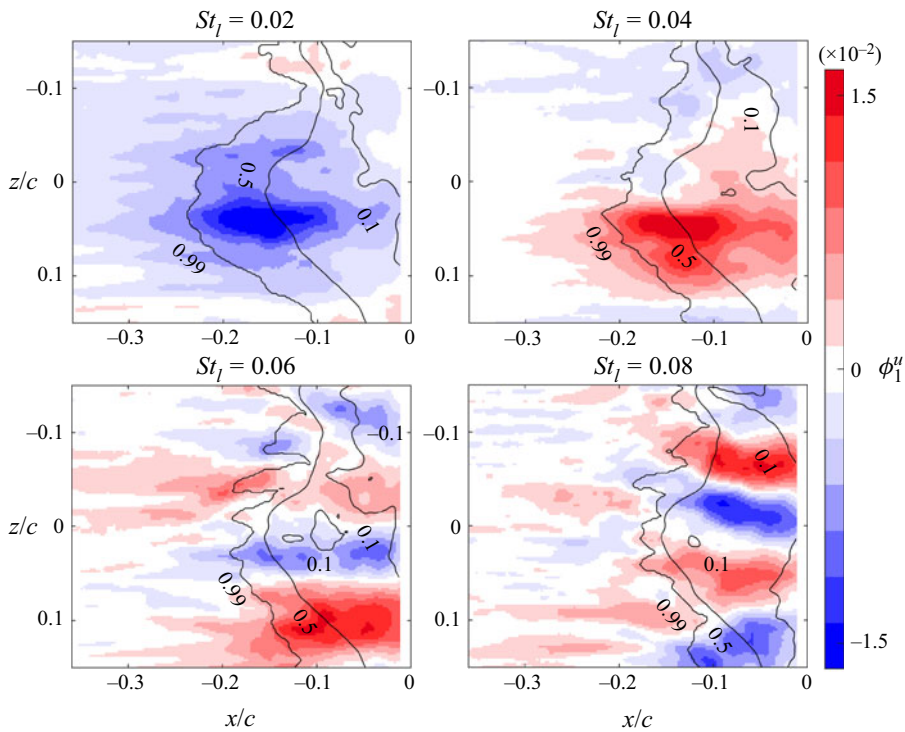


Figure 14. The spatial structures of the first SPOD mode of the streamwise–spanwise PIV plane at $St_l = 0.02$, 0.04 , 0.06 and 0.08 . The contour lines represent the forward-flow probability obtained from the ROM following (6.1).

results in large expansion/contraction of the separation front. The forward-flow probability contours at these St_l values show large advancement/recession of the back-flow region. The spatial patterns at higher St_l of 0.04 and 0.06 consist of smaller alternating structures. However, their forward-flow probability contours still show considerable advancing and receding motions of the back-flow region. Therefore, the lead SPOD mode at the energetic frequencies with $St_l < 0.1$ captures large-scale back-and-forth motions of the separation front.

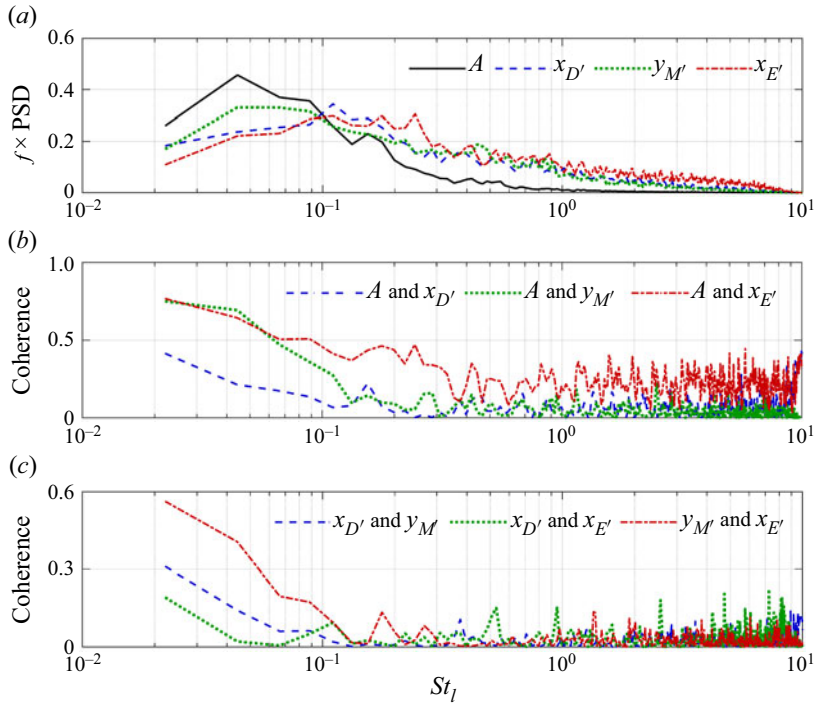


Figure 15. (a) Pre-multiplied PSD of the fluctuations in A , $x_{D'}$, $x_{E'}$ and $y_{M'}$. (b) The coherence functions between A and the three TSB coordinates $x_{D'}$, $x_{E'}$ and $y_{M'}$. (c) The coherence between $x_{D'}$, $x_{E'}$ and $y_{M'}$.

7. The breathing motion

The breathing motion of the TSB is investigated in figure 15(a) using the pre-multiplied PSD of the instantaneous back-flow area, A , computed using the streamwise–wall-normal cross-section of the TSB. The figure also shows the pre-multiplied PSD of the streamwise location of the detachment point ($x_{D'}$), the streamwise location of the endpoint ($x_{E'}$) and the wall-normal location of the midpoint ($y_{M'}$). The coordinates of points D' , E' and M' are also obtained from the instantaneous streamwise–wall-normal PIV plane. The streamwise location of M' is fixed at $x_{M'} = \frac{1}{2} \times (x_D + x_E)$, which is the midpoint between the detachment and endpoints of the mean TSB, while its wall-normal location ($y_{M'}$) is detected from the instantaneous boundary of the TSB. Here, M' is investigated to characterize the flapping motion, i.e. the wall-normal motion of the shear layer. Before calculating the PSDs, the mean value of each variable was subtracted and then it was normalized using its standard deviation, σ . As a result, the area under each curve in figure 15 is equal to one. Similar to the procedure applied for obtaining figure 6, the PSDs were calculated using 45 periodograms (each of the 15 datasets were divided into 3 segments with 50% overlap).

The pre-multiplied PSD of A shows a large peak at approximately $St_l = 0.05$. The peak indicates expansions and contractions of the TSB area at low St_l , which is attributed to the breathing motion. The pre-multiplied PSD of A rapidly decreases at higher St_l and therefore the energetic expansions and contractions of the TSB area are limited to $St_l < 0.1$. The pre-multiplied PSD of $x_{D'}$ shows a broader range of energetic fluctuations with a peak approximately at $St_l = 0.1$. The broader energy distribution in the pre-multiplied PSD of $x_{D'}$ is attributed to the superposition of the small- and large-scale motion of the separation

front seen in the spatial pattern of the SPOD modes of [figure 14](#). The pre-multiplied PSD of $x_{E'}$ also has a broad energy distribution while it exhibits a higher energy at frequencies within the $St_l = 0.1$ to 0.3 range. The latter is slightly smaller than the vortex shedding St_l (from 0.2 to 0.8 based on [figure 6](#)). The discrepancy is associated with the interaction of the two shear layers, making the larger displacements of the endpoint to occur at the lower frequencies. The pre-multiplied PSD of $y_{M'}$ is similar to that of A with most of the energy at lower frequencies. The peak value is also at approximately $St_l = 0.05$ which is similar to the St_l of the breathing motion. This observation suggests that the expansions and contractions of the TSB at $St_l = 0.05$ should correlate with the flapping motion of the shear layer.

To further substantiate the above observations, the correlation between A and $x_{D'}$, $x_{E'}$ and $y_{M'}$ is quantified using the coherence functions shown in [figure 15\(b\)](#). The results show that the coherence function of A and $x_{D'}$ is relatively small across the investigated spectrum. This shows that the breathing motion does not strongly correlate with the motions of the detachment point. In contrast, the coherence of A and $y_{M'}$, and the coherence of A and $x_{E'}$, are large in the low-frequency range of $St_l < 0.1$. Therefore, the breathing motion correlates with both the flapping motion of the shear layer and the streamwise displacements of the TSB endpoint. The correlation between A and $y_{M'}$ was suggested based on [figure 15\(a\)](#) as both signals had high energy and similar pre-multiplied PSD shapes at $St_l < 0.1$. However, the correlation of A and $x_{E'}$ was not expected from [figure 15\(a\)](#) since the pre-multiplied PSD of $x_{E'}$ did not exhibit large energy at $St_l < 0.1$. [Figure 15\(b\)](#) also shows that coherence between A and y_M rapidly declines with increasing St_l , while A and $x_{E'}$ remain relatively correlated at higher frequencies. The coherence function of A and $x_{E'}$ has a local peak at St_l of approximately 0.2 , which overlaps with the peak energy observed in the pre-multiplied PSD of $x_{E'}$ of [figure 15\(a\)](#). In summary, the results show that the breathing motion (low-frequency expansion and contraction of the TSB cross-section in the streamwise–wall-normal plane) correlates with the shear-layer flapping and the displacements of the TSB endpoint.

The coherence functions between $x_{D'}$, $y_{M'}$ and $x_{E'}$ displacements are also investigated in [figure 15\(c\)](#). The results show that the detachment point, $x_{D'}$, does not correlate with the shear-layer flapping, $y_{M'}$, and the TSB endpoint, $x_{E'}$. This agrees with the previous observations that indicated the displacement of the detachment point are derived by the fluctuations of the upcoming TBL (Eich & Kähler 2020; Ma *et al.* 2020). [Figure 15\(c\)](#) also indicates that flapping motion of the shear layer correlates with the streamwise displacements of the endpoint at the low-frequency range of the spectrum.

The results showed that the large-scale expansion and contraction of the TSB area in the streamwise–wall-normal plane are mainly due to the oscillation of the endpoint and the wall-normal flapping of the TSB midpoint. In contrast, the motion of the detachment point has a smaller effect. However, the expansion and contraction of the TSB mainly occur at $St_l = 0.05$, which is smaller than the frequency of energetic motions of the detachment point at $St_l = 0.1$ to 0.3 ([figure 15](#)) or the vortex shedding frequency at $St_l = 0.2$ to 0.8 ([figure 6](#)). This discrepancy is associated with the spatial-averaging effect of the TSB. The mechanism is shown in [figure 16](#) by plotting the pre-multiplied PSD of pointwise and spatially averaged streamwise velocity fluctuations along the shear layers. The pre-multiplied PSD of u at $(x, y) = (0, 3.3\delta_0)$ corresponds to a single point in the upper shear layer, above the TE. As it is observed, the energetic flow motions are at $0.2 < St_l < 1$, which is consistent with the energetic motions seen in [figure 6\(b\)](#). The lines labelled as $k = 0.5$, 1 and 1.5 show the pre-multiplied PSD of streamwise velocity that is spatially averaged along the upper shear layer over a curvilinear trajectory that is centred at

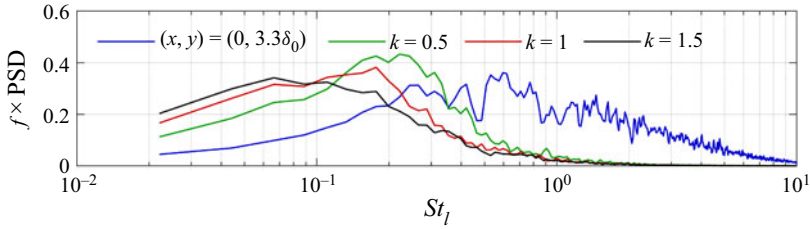


Figure 16. Pre-multiplied PSD of streamwise velocity fluctuations at $(x, y) = (0, 3.3\delta_0)$ and pre-multiplied PSD of spatially averaged velocity according to (7.1).

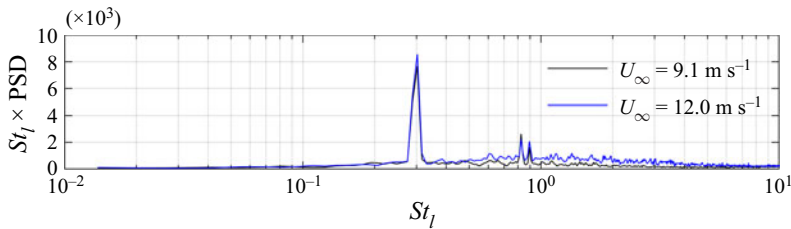


Figure 17. Pre-multiplied PSD of free-stream velocity measured using a hot-wire anemometer in the empty test section of the wind tunnel.

$(x, y) = (0, 3.3\delta_0)$ and extends in the upstream and downstream directions by $0.5l$, $1l$ and $1.5l$, respectively. Therefore, a spatially averaged velocity is first calculated as

$$u_{avg} = \int_{-kl}^{+kl} u \, dx_c, \quad (7.1)$$

and then its pre-multiplied PSD is calculated. In this equation, x_c is the curvilinear coordinate system defined in figure 4(a), and k is the kernel of the averaging line ($k = 0.5$, 1 , and 1.5 in figure 16). The results show that by spatially averaging the velocity fluctuation the St_l of the energetic motions reduces to $St_l = 0.2$ for $k = 0.5$, and finally to a small St_l of 0.07 for $k = 1.5$. Therefore, figure 16 demonstrates that, although the vortex shedding process is at a higher St_l of 0.2 to 0.8 , the ensemble effect of the velocity fluctuations along the shear layer is at a smaller St_l . This observation also suggests that the St_l of the breathing motion inversely scales with the TSB size; the larger the TSB, the greater is the effect of spatial averaging. This is consistent with the investigation of Le Floc'h *et al.* (2020) where three TSBs with small, medium and large sizes were investigated. Their measurements show that the larger TSB has the smallest breathing frequency, which is potentially due to spatial averaging of the velocity fluctuations over a longer shear layer.

8. Summary and conclusions

The TSB formed upstream of the TE of a 2-D wing was experimentally investigated. The wing was made from a NACA 4418 airfoil profile with a chord length, c , of 0.975 m and was set to an angle of attack of 9.7° . The Reynolds number based on c and the free-stream velocity was $720\,000$. The transition of the boundary layer to turbulence was forced using a trip wire placed $0.2c$ downstream of the wing leading edge. Measurements using time-resolved planar PIV were conducted in a large streamwise-wall-normal plane at the midspan of the wing using three synchronized high-speed cameras. The PIV

measurements in a streamwise–spanwise plane that was parallel to and near the wing surface was also carried out using two synchronized high-speed cameras.

The PIV measurements showed that a TBL formed on the suction side of the wing. At $0.35c$ upstream of the TE, the Reynolds number of the TBL based on the free-stream velocity and the local momentum thickness was 2800, and the estimated friction Reynolds number, Re_{τ} , was 900. Farther downstream, the TBL detached due to an APG. The mean detachment point of the TSB was $0.13c$ upstream of the TE. The TSB had a triangular shape skewed in the downstream direction. The size of the TSB was characterized using the length of its upper edge, l , which was equal to $0.16c$. The three vertices of the triangular-shaped TSB consisted of (a) an intermittent detachment point, (b) an approximately fixed corner near the airfoil TE and (c) an intermittent endpoint in the wake region of the airfoil. The TSB featured two strong shear layers: an upper shear layer formed by the intermittent detachment of the suction-side TBL and a lower shear layer formed by the fixed detachment of the pressure-side boundary layer at the airfoil TE. The two shear layers generated zones of high Reynolds stress with peak intensities located downstream of the TE. The shear layers evolved in the wake region (free from the wall) and tended to gradually merge. The triangular shape of the TSB and the presence of the two shear layers differentiates this TSB from the dome-shaped TSB of previous investigations where a single TBL separates and reattaches over a flat plate. In the streamwise–spanwise plane, the TSB featured an undulating separation front.

Spectral analysis of the streamwise velocity fluctuations showed three energetic regions with different Strouhal numbers, St_l , defined as fl/U_{∞} . The first region consisted of the energetic motions of the upstream TBL. The TBL fluctuations started with a large $St_l = 4$ which gradually reduced to $St_l = 0.1$ as the TBL approached the detachment point. These fluctuations were attributed to the LSM of the TBL, whose time scale gradually increased under the effect of the APG. The second energetic region was at the TSB location and featured motions at smaller St_l ranging from 0.03 to 0.08. The peak of these energetic motions was at $St_l = 0.06$. The third region included the energetic motions of the two shear layers at $St_l = 0.2$ to 0.8, which is equivalent to $St_{\delta} = 0.05$ to 0.2. Here, St_{δ} is defined as $f\delta/U_{\infty}$ where δ is the thickness of the shear layer at $x/c = 0.2$ in the wake. The St_{δ} of the fluctuations is consistent with the vortex shedding frequency of Kelvin–Helmholtz instabilities.

The spatial and temporal scales of the low-frequency energetic motions within the TSB were investigated using instantaneous visualizations and two-point correlations. The results show that the TSB consisted of large zones of positive and negative streamwise velocity fluctuation. The zones were several times wider than the LSM within the upstream TBL. The time scale of these zones was also two orders of magnitude greater than the LSM within the upstream TBL. This observation agrees with the smaller $St_l = 0.03$ to 0.08 observed within the TSB relative to the higher $St_l = 0.1$ to 4.0 within the TBL. The positive and negative zones modulated the location of the separation front. Zones with positive fluctuating velocity appeared when the detachment point shifted in the downstream direction, while zones with negative fluctuating velocity were present when the detachment point shifted in the upstream direction. Analysis of the mean flow field suggested that these large zones are formed by the Görtler structures as the flow follows the curved streamlines above the TSB. The two-point correlation functions showed that the zones strongly correlate with the velocity fluctuations between the two shear layers in the wake region.

Spectral proper orthogonal decomposition was performed to identify the energetic motions of the TSB. In the streamwise–wall-normal plane, the dominant SPOD mode

captured a large-scale breathing motion at $St_l = 0.02$. The first mode also showed the vortex shedding processes at $St_l = 0.16$ and 0.72 . The vortex shedding process at $St_l = 0.16$ contributed to the intermittency of the TSB aft section, while no considerable intermittency was observed at $St_l = 0.72$. In the streamwise–spanwise plane, the SPOD modes had a higher energy at the lower frequencies. The dominant SPOD mode demonstrates large-scale advancement/recessions of the TSB region at $St_l < 0.1$.

Spectral analysis of the TSB cross-section in the streamwise–wall-normal plane showed that the TSB expands and contracts (breathes) at a frequency of $St_l = 0.05$. Analysis using the coherence function confirmed that the TSB breathing correlates with the motion of the TSB endpoint and the wall-normal motion (flapping) of the upper shear layer. As a result, the breathing of the TSB was mainly attributed to the shear-layer motion and the vortex shedding fluctuation. The lower frequency of the breathing motion with respect to the fervency of the vortex shedding process was attributed to the spatial-averaging effect of the TSB. The intermittency of the detachment point showed broad fluctuations within $0.01 < St_l < 0.2$ with no strong correlation with the cross-sectional area of the TSB.

Supplemental movies. Supplementary movies are available at <https://doi.org/10.1017/jfm.2022.603>.

Funding. We acknowledge the support of Future Energy Systems (project T14-P05) at the University of Alberta.

Declaration of interests. The authors report no conflict of interests.

Author ORCID.

© Sina Ghaemi <https://orcid.org/0000-0001-8893-2993>.

Appendix

The PSD of the free-stream velocity is shown in [figure 17](#) to characterize the frequency of its fluctuations. The velocity signal was measured using a hot-wire anemometer in the empty test section of the wind tunnel at mean velocities of 9.1 and 12.0 m s^{-1} . The details of the measurement procedure are available in Gibeau *et al.* (2020). The PSD shows an energetic peak at $St_l = 0.3$, and smaller peaks at St_l of approximately 0.8 – 0.9 . For consistency, the St_l is calculated here based on the mean length of the separation bubble, l , which is equal to $0.16c$.

REFERENCES

- ADRIAN, R.J., MEINHART, C.D. & TOMKINS, C.D. 2000 Vortex organization in the outer region of the turbulent boundary layer. *J. Fluid Mech.* **422**, 1–54.
- BALAKUMAR, B.J. & ADRIAN, R.J. 2007 Large-and very-large-scale motions in channel and boundary-layer flows. *Phil. Trans. R. Soc. A: Math. Phys. Engng Sci.* **365** (1852), 665–681.
- BROEREN, A. & BRAGG, M. 1998 Low-frequency flowfield unsteadiness during airfoil stall and the influence of stall type. In *16th AIAA Applied Aerodynamics Conference, AIAA Paper 1998-2517*.
- CASTRO, I.P. 1981 Measurements in shear layers separating from surface-mounted bluff bodies. *J. Wind Engng Indus. Aerodyn.* **7** (3), 253–272.
- CASTRO, I.P. & HAQUE, A. 1987 The structure of a turbulent shear layer bounding a separation region. *J. Fluid Mech.* **179**, 439–468.
- CHERRY, N.J., HILLIER, R. & LATOUR, M.E.M.P. 1984 Unsteady measurements in a separated and reattaching flow. *J. Fluid Mech.* **144**, 13–46.
- CICATELLI, G. & SIEVERDING, C.H. 1997 The effect of vortex shedding on the unsteady pressure distribution around the trailing edge of a turbine blade. *Trans. ASME J. Turbomach.* **119**, 810–819.
- CLEMENS, N.T. & NARAYANASWAMY, V. 2014 Low-frequency unsteadiness of shock wave/turbulent boundary layer interactions. *Annu. Rev. Fluid Mech.* **46**, 469–492.

Unsteady motions in the turbulent separation bubble

- DELL'ORSO, H. & AMITAY, M. 2018 Parametric investigation of stall cell formation on a NACA 0015 airfoil. *AIAA J.* **56** (8), 3216–3228.
- DELL'ORSO, H., TUNA, B.A. & AMITAY, M. 2016 Measurement of three-dimensional stall cells on a two-dimensional NACA0015 airfoil. *AIAA J.* **54** (12), 3872–3883.
- DIANAT, M. & CASTRO, I.P. 1991 Turbulence in a separated boundary layer. *J. Fluid Mech.* **226**, 91–123.
- DOLLING, D.S. 2001 Fifty years of shock-wave/boundary-layer interaction research: what next? *AIAA J.* **39** (8), 1517–1531.
- DRIVER, D.M., SEEGMILLER, H.L. & MARVIN, J.G. 1987 Time-dependent behavior of a reattaching shear layer. *AIAA J.* **25** (7), 914–919.
- DUSSAUGE, J.P., DUPONT, P. & DEBIÈVE, J.F. 2006 Unsteadiness in shock wave boundary layer interactions with separation. *Aerosp. Sci. Technol.* **10** (2), 85–91.
- EATON, J.K. 1980 *Turbulent Flow Reattachment: An Experimental Study of the Flow and Structure Behind a Backward-Facing Step*. PhD Thesis, Stanford University.
- EATON, J.K. & JOHNSTON, J.P. 1982 Low frequency unsteadiness of a reattaching turbulent shear layer. In *Turbulent Shear Flows*, vol. 3, pp. 162–170. Springer.
- EICH, F. & KÄHLER, C.J. 2020 Large-scale coherent motions in turbulent boundary layers under an adverse pressure gradient up to flow separation. *Intl J. Heat Fluid Flow* **85**, 108645.
- FANG, X. & TACHIE, M.F. 2020 Spatio-temporal dynamics of flow separation induced by a forward-facing step submerged in a thick turbulent boundary layer. *J. Fluid Mech.* **892**, A40.
- FLORYAN, J.M. 1991 On the Görtler instability of boundary layers. *Prog. Aerosp. Sci.* **28** (3), 235–271.
- FORLITI, D.J., TANG, B.A. & STRYKOWSKI, P.J. 2005 An experimental investigation of planar countercurrent turbulent shear layers. *J. Fluid Mech.* **530**, 241–264.
- GANAPATHISUBRAMANI, B., CLEMENS, N.T. & DOLLING, D.S. 2009 Low-frequency dynamics of shock-induced separation in a compression ramp interaction. *J. Fluid Mech.* **636**, 397–415.
- GANAPATHISUBRAMANI, B., HUTCHINS, N., HAMBLETON, W.T., LONGMIRE, E.K. & MARUSIC, I. 2005 Investigation of large-scale coherence in a turbulent boundary layer using two-point correlations. *J. Fluid Mech.* **524**, 57–80.
- GHAEMI, S., RAGNI, D. & SCARANO, F. 2012 PIV-based pressure fluctuations in the turbulent boundary layer. *Exp. Fluids* **53** (6), 1823–1840.
- GIBEAU, B., GINGRAS, D. & GHAEMI, S. 2020 Evaluation of a full-scale helium-filled soap bubble generator. *Exp. Fluids* **61** (2), 28.
- GÖRTLER, H. 1954 On the three-dimensional instability of laminar boundary layer on concave walls. In *National Advisory Committee for Aeronautics*, NACA Tech. Memo. 1375.
- GUALA, M., HOMMEMA, S.E. & ADRIAN, R.J. 2006 Large-scale and very-large-scale motions in turbulent pipe flow. *J. Fluid Mech.* **554**, 521–542.
- HUMBLE, R.A., SCARANO, F. & VAN OUDHEUSDEN, B.W. 2009 Unsteady aspects of an incident shock wave/turbulent boundary layer interaction. *J. Fluid Mech.* **635**, 47–74.
- HUTCHINS, N. & MARUSIC, I. 2007 Evidence of very long meandering features in the logarithmic region of turbulent boundary layers. *J. Fluid Mech.* **579**, 1–28.
- KIYA, M. & SASAKI, K. 1983 Structure of a turbulent separation bubble. *J. Fluid Mech.* **137**, 83–113.
- KIYA, M. & SASAKI, K. 1985 Structure of large-scale vortices and unsteady reverse flow in the reattaching zone of a turbulent separation bubble. *J. Fluid Mech.* **154**, 463–491.
- LE FLOC'H, A., WEISS, J., MOHAMMED-TAIFOUR, A. & DUFRESNE, L. 2020 Measurements of pressure and velocity fluctuations in a family of turbulent separation bubbles. *J. Fluid Mech.* **902**, A13.
- LEE, J.H. & SUNG, H.J. 2009 Structures in turbulent boundary layers subjected to adverse pressure gradients. *J. Fluid Mech.* **639**, 101–131.
- LOUCKS, R.B. & WALLACE, J.M. 2012 Velocity and velocity gradient based properties of a turbulent plane mixing layer. *J. Fluid Mech.* **699**, 280–319.
- MA, A., GIBEAU, B. & GHAEMI, S. 2020 Time-resolved topology of turbulent boundary layer separation over the trailing edge of an airfoil. *J. Fluid Mech.* **891**, A1.
- MAULL, D.J. & YOUNG, R.A. 1973 Vortex shedding from bluff bodies in a shear flow. *J. Fluid Mech.* **60** (2), 401–409.
- MOHAMMED-TAIFOUR, A. & WEISS, J. 2016 Unsteadiness in a large turbulent separation bubble. *J. Fluid Mech.* **799**, 383–412.
- MOHAMMED-TAIFOUR, A. & WEISS, J. 2021 Periodic forcing of a large turbulent separation bubble. *J. Fluid Mech.* **915**, A24.
- MONKEWITZ, P.A. & HUERRE, P. 1982 Influence of the velocity ratio on the spatial instability of mixing layers. *Phys. Fluids* **25** (7), 1137–1143.

- NA, Y. & MOIN, P. 1998 Direct numerical simulation of a separated turbulent boundary layer. *J. Fluid Mech.* **374**, 379–405.
- OZKAN, G.M. 2021 Control of the flow in the near wake of an airfoil at full stall using fixed trailing-edge plates. *Exp. Therm. Fluid Sci.* **122**, 110296.
- PATRICK, W.P. 1987 Flowfield measurements in a separated and reattached flat plate turbulent boundary layer. *NASA Tech. Rep.* 4052.
- PEARSON, D.S., GOULART, P.J. & GANAPATHISUBRAMANI, B. 2013 Turbulent separation upstream of a forward-facing step. *J. Fluid Mech.* **724**, 284–304.
- PIPONNAU, S., DUSSAUGE, J.P., DEBIEVE, J.F. & DUPONT, P. 2009 A simple model for low-frequency unsteadiness in shock-induced separation. *J. Fluid Mech.* **629**, 87–108.
- SCHLATTER, P. & ÖRLÜ, R. 2010 Assessment of direct numerical simulation data of turbulent boundary layers. *J. Fluid Mech.* **659**, 116–126.
- SCHMIDT, O.T., TOWNE, A., RIGAS, G., COLONIUS, T. & BRÈS, G.A. 2018 Spectral analysis of jet turbulence. *J. Fluid Mech.* **855**, 953–982.
- SIGURDSON, L.W. 1995 The structure and control of a turbulent reattaching flow. *J. Fluid Mech.* **298**, 139–165.
- SKOTE, M. & HENNINGSON, D.S. 2002 Direct numerical simulation of a separated turbulent boundary layer. *Trans. ASME J. Fluids Engng* **471**, 107–136.
- TOWNE, A., SCHMIDT, O.T. & COLONIUS, T. 2018 Spectral proper orthogonal decomposition and its relationship to dynamic mode decomposition and resolvent analysis. *J. Fluid Mech.* **847**, 821–867.
- WANG, S. & GHAEMI, S. 2021 Full-span topology of trailing-edge separation at different angles of attack. *AIAA J.* **59**, 5186–5197.
- WEIHS, D. & KATZ, J. 1983 Cellular patterns in poststall flow over unswept wings. *AIAA J.* **21** (12), 1757–1759.
- WEISS, J., MOHAMMED-TAIFOUR, A. & SCHWAAB, Q. 2015 Unsteady behavior of a pressure-induced turbulent separation bubble. *AIAA J.* **53** (9), 2634–2645.
- WESTERWEEL, J. & SCARANO, F. 2005 Universal outlier detection for PIV data. *Exp. Fluids* **39** (6), 1096–1100.
- WU, M. & MARTIN, M.P. 2008 Analysis of shock motion in shockwave and turbulent boundary layer interaction using direct numerical simulation data. *J. Fluid Mech.* **594**, 71–83.
- WU, W., MENEVEAU, C. & MITTAL, R. 2020 Spatio-temporal dynamics of turbulent separation bubbles. *J. Fluid Mech.* **883**, A45.
- WU, W. & PIOMELLI, U. 2018 Effects of surface roughness on a separating turbulent boundary layer. *J. Fluid Mech.* **841**, 552–580.
- YOU, J., BUCHTA, D.A. & ZAKI, T.A. 2021 Concave-wall turbulent boundary layers without and with free-stream turbulence. *J. Fluid Mech.* **915**, A4.
- ZAMAN, K.B.M.Q., MCKINZIE, D.J. & RUMSEY, C.L. 1989 A natural low-frequency oscillation of the flow over an airfoil near stalling conditions. *J. Fluid Mech.* **202**, 403–442.